IEEE Transactions on Robotics (T-RO) paper, presented at ICRA 2026, Vienna, Austria. Cite as T-RO paper.

Knee-Inspired Hinge Absorbs Longitudinal Impacts to Enhance Robot-Environment Interaction Safety

Lianxin Yang, *Member, IEEE*, Xinyan Li, Tianyu Zhao, and Zhihua Zhao

***Abstract*—As robots integrate into human society, ensuring safe robot-environment interaction, particularly in the event of collisions, has emerged as a growing design priority. A promising solution is introducing proper compliance into existing rigid robots, akin to musculoskeletal systems, to absorb impacts in various directions. However, mimicking longitudinal compliance seen in biological joints to absorb compressive impacts along limbs, such as the role of cartilages like menisci, remains a challenge shadowed by the complexity of joint architecture. Here, exploring and adapting the elastic longitudinal movement structure of knee, we incorporated traditional mechanical hinges with a compact buffer structure to enable both simple rotational motion and effective longitudinal impact absorption. Under longitudinal loading, the buffer structure functions as a mechanism transmitting the limited compression to amplified deformations of elastic elements, thus producing resistance against load. The resistive load-displacement relationship is tailorable by tuning diverse elastic components, allowing for a high-static-low-dynamic stiffness to improve energy absorption efficiency. Drop tests and walking robot demonstrations confirm that the proposed knee-inspired hinge not only mitigates acceleration transmitted to the robot's main body but also reduces ground reaction forces, thereby improving robot-environment interaction safety. This work highlights the design paradigm of adapting natural solutions to mechanical systems, and holds potential for direct integration into diverse robots, exoskeletons, and prostheses.**

***Index Terms*—Biomimetics, compliant joint/mechanism, impact absorption, physical human–robot interaction.**

I. Introduction

VERTEBRATE animals, empowered by their biological structures and nuanced motor control systems [1], [2], [3], [4], [5], [6], achieve not only diverse functions like agile locomotion across complex terrains [7], [8], but also safe interactions with environment by attenuating unnecessary dynamic forces in multiple directions [9], [10], [11]. While state-of-art robots have accomplished diverse tasks in laboratories thanks to advances in intelligent active control [12], [13], [14], [15], their interaction with human society remains challenging due to the inherent structure rigidity, especially in working conditions accompanying collisions [16], [17], [18], [19], [20]. Consequently, developing articulated soft robots capable of absorbing impacts in various directions [21], [22], thus protecting both the robot and its surroundings, has attracted growing attention.

Current designs for articulated soft robots are primarily inspired by the musculoskeletal structures of vertebrates, especially humans, where rigid bones are articulated by intricate joints with flexible tendons and muscles [23], [24], [25], [26], and cartilages like menisci [27], [28], [29], [30]. These efforts can be roughly categorized into two paradigms: one aims to replicate the complex architecture of its biological counterpart, including artificial muscles [31], [32], [33], [34], [35], tendons [36], and biomimetic joints [37], [38], while the other seeks to identify the key physics of its functions and adapt them into simplified structures to fit traditional robotic frameworks. Iconic examples of the former paradigm are anthropomorphic joints [39], [40], mimicking human knees, where an open joint is complemented by artificial menisci. These structures allow for both rotation and limited longitudinal movement along bones through flexible deformation of the menisci, thereby attenuating rotational torque and longitudinal forces during impacts. However, the open architecture of such designs poses potential structural stability issues, hindering their integration with existing robotic systems at present stage.

The second design paradigm—the "understanding-to-building" approach, just hits the point of this compatibility issue. Inheriting the traditional robotic framework actuated by motors, conventional elastic elements, such as springs and rubber bands, are incorporated to create elastic actuators [41], [42], [43], [44], [45] or spring-linkage systems [46], [47], [48], functioning similarly to human muscles and tendons. With rigid hinges articulating the rigid links, these designs finally absorb rotational impacts at joints. However, the longitudinal force along links, which is a major component in functionalities like walking, propagates without attenuation due to the high contact stiffness in joints. Hence, it is natural to raise the question: Could longitudinal compliance be integrated into traditional mechanical hinges to function like the built-in compliant structures found in biological joints, such as the knees, where skeletal constraints effectively combine with impact mitigation?

Here, combining traditional mechanical hinges and biological knee joints, as shown in Fig. 1, we developed a knee-inspired

Received 18 August 2025; accepted 19 November 2025. Date of publication 25 November 2025; date of current version 11 December 2025. This work was supported in part by the National Natural Science Foundation of China under Grant 12202226 and Grant 12272198, and in part by the China Postdoctoral Science Foundation under Grant 2022M711831. This article was recommended for publication by Associate Editor M. Tanaka and Editor E. De Momi upon evaluation of the reviewers' comments. *(Corresponding author: Zhihua Zhao.)*

Lianxin Yang is with the School of Automation Science and Electrical Engineering, Beihang University, Beijing 100191, China, and also with the School of Aerospace Engineering, Tsinghua University, Beijing 100084, China (e-mail: yanglx@buaa.edu.cn).

Xinyan Li, Tianyu Zhao, and Zhihua Zhao are with the School of Aerospace Engineering, Tsinghua University, Beijing 100084, China (e-mail: zhaozh@tsinghua.edu.cn).

This article has supplementary downloadable material available at https://doi.org/10.1109/TRO.2025.3637130, provided by the authors.

Digital Object Identifier 10.1109/TRO.2025.3637130

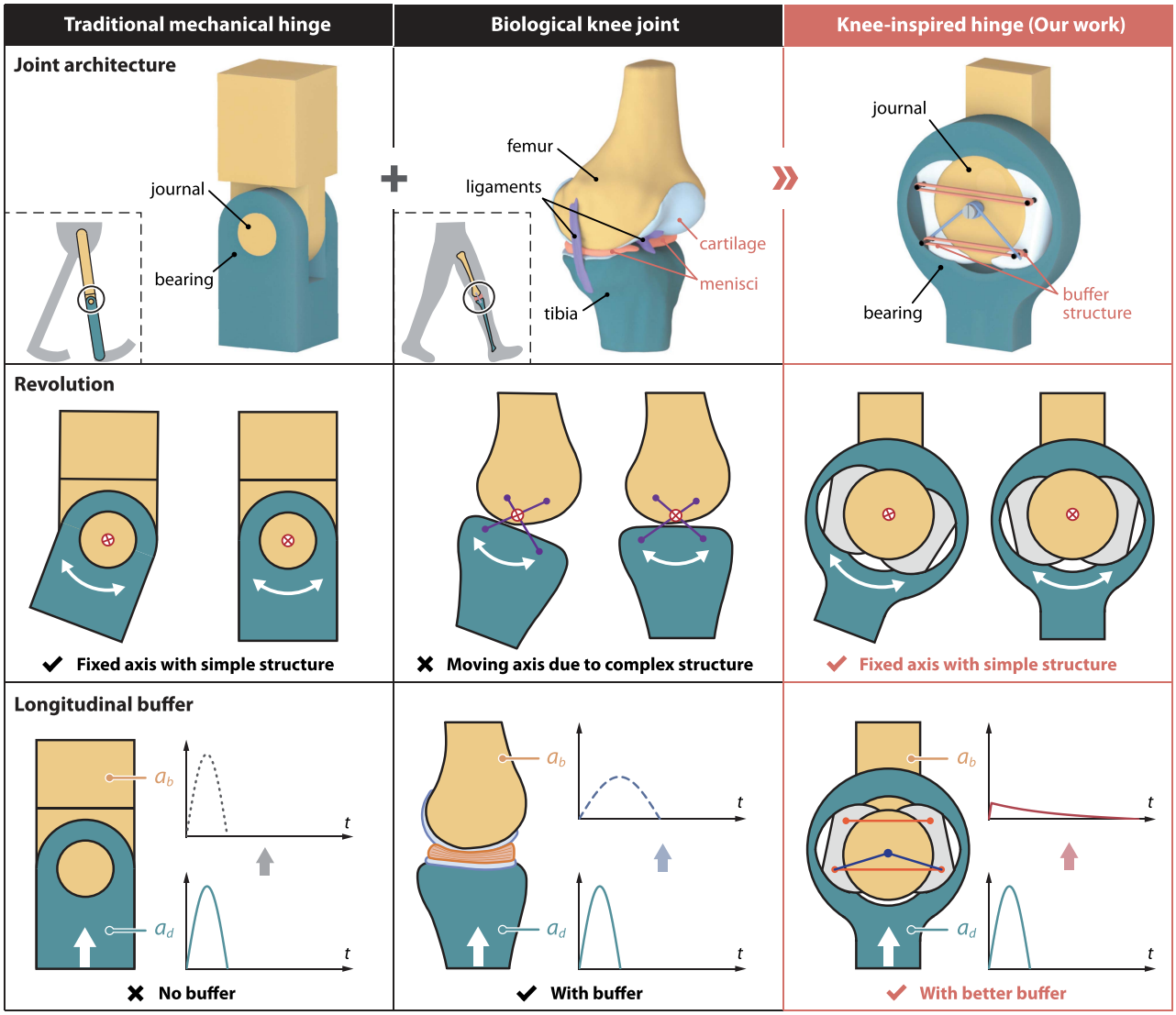

Fig. 1. Concept of the knee-inspired hinge absorbing longitudinal impacts. The proposed joint combines the advantage of traditional mechanical hinges in its simple fixed-axis rotation pattern, and the advantage of biological knee joints in longitudinal compliance for buffering.

hinge—a compact revolute joint with longitudinal compliance absorbing compressive impacts along articulated links. Instead of simply replicating a biological joint, we adapted the human knee structure, based on our understanding of its impact attenuation mechanisms, to fit the architecture of traditional mechanical hinge, empowering it with longitudinal buffering capability. Evolved from traditional mechanical hinges, our bioinspired hinges inherit the simple structure and the fixed-axis rotation pattern, where the bearing rotates about the central axis of the circular journal. As a comparison, biological knee joints undergo complex kinematics with a moving instant rotation center, constrained by its intricate geometry coupled with ligaments [49], [50]. While the journal and bearing in traditional mechanical hinges are in direct contact with each other, resulting in high longitudinal stiffness of linkage and ignorable impact attenuation [51], our knee-inspired hinge inserts a buffer structure within the joint clearance, working like the menisci absorbing longitudinal impacts along links, but with geometry specially designed to fit the architecture of mechanical hinges. By combining the advantages of both mechanical hinges and biological joints, our knee-inspired hinges can directly replace traditional hinges in robotic systems, offering a simple and effective solution to enhance interaction safety with the environment, thus accelerating the integration of robots into society.

The rest of this article is organized as follows. Section II introduces the structure and geometry design of the knee-inspired hinge. Section III characterizes the tailorable longitudinal load-displacement relationship. Section IV evaluates the impact absorption performance with drop tests. Section V demonstrates the enhancement of interaction safety in a biped walking robot. Finally, Section VI concludes this article.

II. Knee-Inspired Hinge With Buffer Structure

A. Overall Structure

As shown in Fig. 2(a)–(b), our knee-inspired hinge modifies traditional mechanical hinges by filling the clearance between the journal and bearing with a buffer structure. This buffer

IEEE Transactions on Robotics (T-RO) paper, presented at ICRA 2026, Vienna, Austria. Cite as T-RO paper.

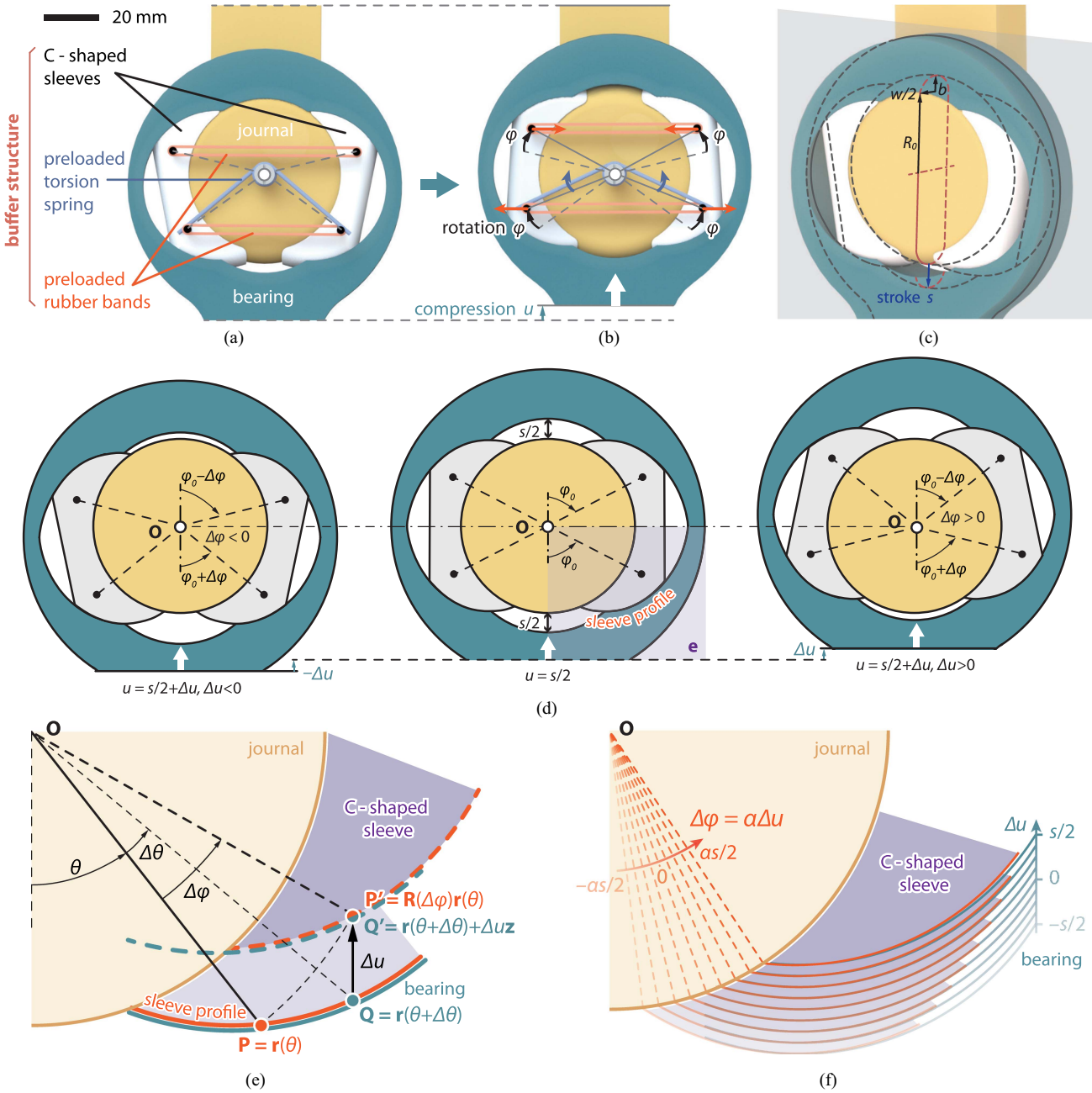

Fig. 2. Structure and geometry of the knee-inspired hinge. (a) Structure of the knee-inspired hinge, illustrated by a CAD model. (b) Overview of the passive response to longitudinal compression. Black arrows indicate rotations of C-shaped sleeves. Red and blue arrows indicate induced deformations of rubber bands and torsion spring, respectively. (c) Geometry design of the knee-inspired joint. Red and gray lines indicate radial section and sagittal section, respectively. (d) Kinematics of the planar motion, described with any sagittal section. (e) Design of sleeve profile. Red and cyan lines indicate the bottom profile of C-shaped sleeve and the profile of bearing, conforming to each other after a rotation of $\Delta\varphi$ or a translation of Δu, respectively. Solid lines indicate the profile corresponding to the configuration of $u = s/2$ in (d), while dashed lines correspond to $u = s/2 + \Delta u$. (f) Confirmation of conformal condition at different loading phases.

structure consists of a pair of movable rigid C-shaped sleeves with specialized geometry to realize target kinematics, and a set of elastic components, including preloaded torsional spring and rubber bands, to provide restoring forces. When the hinge is subject to a longitudinal load along the link connected to the bearing, the bearing and journal squeeze and separate the C-shaped sleeves, resulting in their symmetrical upward rotation about the journal axis and the deformation of elastic elements to produce a resistive force against the longitudinal compression. This process continues until the compression reaches the maximum stroke, where the journal touches and sticks to bearing, thus degenerating to a traditional mechanical hinge with high contact stiffness and load capacity.

B. Kinematics and Sleeve Profile

Here, the structure was designed to confine the relative motion between the journal and the bearing to a strict planar motion

within the sagittal plane. To achieve this, the sagittal sections of both components feature similar contact profiles, as indicated by the gray dashed lines in Fig. 2(c), while the radial sections form a confined elliptical profile to restrict movement outside the sagittal plane, resulting in high stiffness against axial force and radial moment load, which are comparable to that of a rigid mechanical hinge with same material configuration (see Appendix A for details), to ensure hinge stability. More specifically, Fig. 2(d) details the sagittal section profile and its corresponding kinematics. Under a longitudinal compression, the C-shaped sleeves rotate about the journal center O by an angle φ due to the circular contact interface, while the bearing undergoes longitudinal translation u. During combined rotation φ and compression u, the relative configuration of the contacting interface between the bottom interface of the C-shaped sleeve and the inner surface of the bearing evolves dynamically. To ensure optimal conformity of the contacting interface during loading process, the sleeve profile was designed based on the following detailed geometry and kinematic analysis.

The sleeve profile is expressed in a polar coordinate as $r(\theta)$ for a particular vertically symmetric configuration as shown in the middle of Fig. 2(d), where $u = s/2$, with s representing the maximum compression stroke of the bearing. Referring to this configuration, the C-shaped sleeve rotates by angle $\Delta\varphi$, while the bearing moves upward by Δu. Under this motion, we assume that for any point $\mathbf{P} = \mathbf{r}(\theta)$ at bottom interface of C-shaped sleeve, there is a point $\mathbf{Q} = \mathbf{r}(\theta + \Delta\theta)$ at top interface of bearing in the initial configuration. These points coincide in the deformed configuration as $\mathbf{P}'$ and $\mathbf{Q}'$, as shown in Fig. 2(e). Here, $\mathbf{P}' = \mathbf{R}(\Delta\varphi)\mathbf{r}(\theta)$, where $\mathbf{R}(\Delta\varphi)$ is the 2-D rotation matrix corresponding to the rotation angle $\Delta\varphi$, and $\mathbf{Q}' = \mathbf{r}(\theta + \Delta\theta) + \Delta u\mathbf{z}$, with $\mathbf{z}$ denoting the longitudinal unit vector.

The conformal conditions require $\mathbf{P}' = \mathbf{Q}'$, meaning the sleeve profile $r(\theta)$ and kinematic relationship $\Delta\varphi = \Delta\varphi(\Delta u)$ must satisfy

$$\forall\, \theta, \Delta u \quad \exists\, \Delta\theta \quad \text{s.t. } \mathbf{R}(\Delta\varphi)\mathbf{r}(\theta) = \mathbf{r}(\theta + \Delta\theta) + \Delta u\mathbf{z}. \tag{1}$$

Decomposing this equation along and perpendicular to OQ yields

$$r(\theta + \Delta\theta) - r(\theta)\cos(\Delta\varphi - \Delta\theta) = \Delta u \cos(\theta + \Delta\theta) \tag{2}$$

$$r(\theta)\sin(\Delta\varphi - \Delta\theta) = \Delta u \sin(\theta + \Delta\theta). \tag{3}$$

These nonlinear equations are difficult to solve analytically. Therefore, we seek solutions for small strokes only. We assume Δu, $\Delta\varphi$, and $\Delta\theta$ are small and linearize the equations using a first-order approximation

$$(\mathrm{d}r(\theta)/\mathrm{d}\theta)\,\Delta\theta = \Delta u \cos\theta \tag{4}$$

$$(\Delta\varphi - \Delta\theta)r(\theta) = \Delta u \sin\theta. \tag{5}$$

Eliminating $\Delta\theta$ by combining (4) and (5), we obtain

$$[(\Delta\varphi/\Delta u)r(\theta) - \sin\theta]\,\mathrm{d}r(\theta) - r(\theta)\cos\theta\,\mathrm{d}\theta = 0. \tag{6}$$

For this condition to hold for any Δu and θ, the necessary and sufficient constraints are

$$\Delta\varphi/\Delta u = \alpha = \text{constant} \tag{7}$$

$$\mathrm{d}\left[\alpha r^2(\theta) - 2r(\theta)\sin\theta\right] = 0 \tag{8}$$

where the constant α represents the proportionality between $\Delta\varphi$ and Δu.

Integrating (8), the sleeve profile $r(\theta)$ is determined by

$$r(\theta) = \frac{1}{\alpha}\left(\sin\theta + \sqrt{\sin^2\theta + \alpha^2R^2 - 2\alpha R\sin\theta_0}\right) \tag{9}$$

where (R, θ_0) is the polar coordinate of the intersection between the sleeve profile and circular journal in the sagittal section.

Thus, the designed sleeve profile (9) ensures the conformal condition is maintained throughout the loading process, enforcing the kinematics constraint

$$\Delta\varphi = \alpha\Delta u \tag{10}$$

which establishes a direct proportionality between rotation $\Delta\varphi$ and translation Δu, as expressed in (7).

Fig. 2(f) provides an illustrative example with $\alpha = 3.35^\circ/\text{mm}$, $R = 32.5\,\text{mm}$, and $\theta_0 = 20^\circ$. As compression $u = s/2 + \Delta u$ increases from 0 to the maximum stroke $s = 8\,\text{mm}$ in an interval of 1 mm, $\Delta\varphi$ varies from $-\alpha s/2 = -13.4^\circ$ to $\alpha s/2 = 13.4^\circ$, ensuring that the outer interface of the C-shaped sleeve remains conformal to the bearing, within the accuracy of the first-order approximation.

In summary, the prescribed geometry constrains the C-shaped sleeves to rotate symmetrically about the central axis of the journal in response to longitudinal compression along the link connected to bearing. The rotation angle is linearly related to the longitudinal compression, with the proportionality determined by the geometric parameter of the sleeve profile. This rotation will further cause the deformation of the elastic elements within the buffer structure, shaping the force characteristics under longitudinal loading.

III. Longitudinal Force Tailoring

The elastic elements providing and tailoring the longitudinal resistive force include a pair of preloaded rubber bands with two ends of each fixed on the anchors at the pair of C-shaped sleeves, and a preloaded torsion spring concentric with the journal, with two arms passing through the lower anchors, as shown in Fig. 2(a). The anchors on the C-shaped sleeves all deviate from the vertical axis with the same angle φ_0 at the particular configuration of $u = s/2$, as shown in the middle of Fig. 2(d).

To assess the distinct effects of the two elastic components on the longitudinal force characteristics, prototypes of the knee-inspired hinges with the aforementioned structure and geometry were fabricated. The design parameters are listed in Table I unless otherwise specified, with the rationale for their selection detailed in Appendix B.

To simplify manufacturing, the journal and bearing were fabricated using photosensitive resin (Young's modulus $E = 2.6\,\text{GPa}$) via stereolithography (SLA) 3D printing, a form of additive manufacturing, and then painted in different colors for clarity. The C-shaped sleeves were CNC-machined from polytetrafluoroethylene (PTFE) (Young's modulus $E = 0.6\,\text{GPa}$ and friction coefficient $\mu = 0.05 \sim 0.2$ to different materials) to minimize friction. Rubber bands (3M Unitek) and torsion springs are standard commercial components, which can withstand thousands of cycles without severe change in mechanical properties and are thus widely applied in compliance design [52],

IEEE Transactions on Robotics (T-RO) paper, presented at ICRA 2026, Vienna, Austria. Cite as T-RO paper.

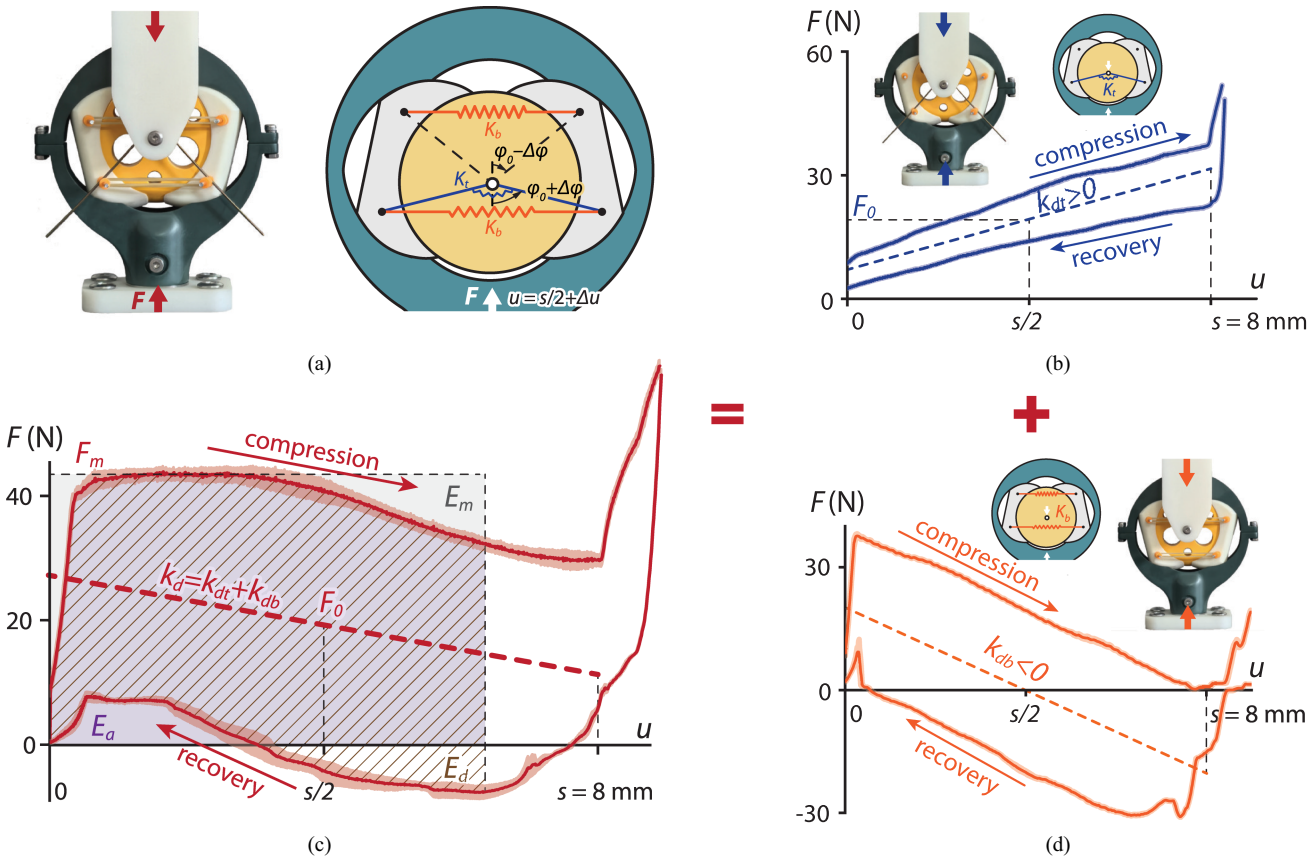

Fig. 3. Longitudinal force characterization of the knee-inspired hinge. (a)–(b) Prototype, model, and load-displacement curve of knee-inspired hinge under longitudinal loading along the link connected to bearing. Gray, purple, and shaded areas indicate the ideal maximum energy absorption E_m, measured energy absorption E_a, and energy dissipation E_d, respectively. (c)—(d) Conditions when only the torsion spring or rubber bands are engaged. In (b)–(d), solid lines indicate the mean measured results of five trials, while surrounding shaded areas indicate ± 1 standard deviation. Dashed lines indicate theoretical predictions for frictionless conditions.

TABLE I
PARAMETER OF KNEE-INSPIRED HINGE

Parameter	Value	Unit
Journal radius R_0	25	mm
Journal thickness w	20	mm
Journal rim radius b	7.5	mm
Maximum stroke s	8	mm
Proportion $\alpha = \Delta\varphi/\Delta u$	3.35	deg/mm
Angular position of buffer θ_0	20	deg
Radial position of anchors R_f	34.5	mm
Angular position of anchors φ_0	65	deg
Torsion spring stiffness K_t	1.95	N mm/deg
Half free angle of torsion spring φ_i	22.5	deg
Rubber band stiffness K_b	0.3	N/mm
Half free length of rubber band L_0	4.75	mm

[53], with parameters selected and tailored to achieve desired force characteristics. Here, we choose rubber bands for convenience to tailor its stiffness and preload. When the design parameter is settled, it could be replaced by a tension spring for a more stable elastic property.

For simplicity and without loss of generality, we primarily discuss the frictionless case in the following analysis, while the effects of friction are addressed separately in Appendix C.

A. Load-Displacement Relationship in Frictionless Conditions

Under frictionless conditions, as depicted in Fig. 3(a), the load-displacement relationship can be derived theoretically using the principle of virtual work, meaning the input energy is stored in the elastic components, expressed as

$$F\delta u = \delta V_t + \delta V_b \tag{11}$$

where F is the longitudinal force, and u is the compression. V_t and V_b represent the elastic potential energy of the torsion spring and rubber bands, respectively. The δ symbol denotes variation.

Given the kinematic relationship $\Delta\varphi = \alpha\Delta u$ from (10), V_t and V_b can be calculated as

$$V_t = \frac{1}{2}K_t(2\varphi_0 + 2\alpha\Delta u - 2\varphi_i)^2 \tag{12}$$

$$V_b = \frac{1}{2}K_b[2R_f\sin(\varphi_0 + \alpha\Delta u) - 2L_0]^2 + \frac{1}{2}K_b[2R_f\sin(\varphi_0 - \alpha\Delta u) - 2L_0]^2 \tag{13}$$

where K_t and K_b are the stiffness of the torsion spring and rubber bands, respectively. φ_i represents the half-angle of the unstressed torsion spring, and L_0 is half-length of the unstretched rubber bands. R_f is the distance from the anchors on the sleeves to the journal center.

By taking variations and then linearizing the equations with respect to Δu, assuming a small working stroke s, the longitudinal force is derived as

$$F = 4\alpha K_t(\varphi_0 - \varphi_i) + 4\alpha^2 K_t(u - s/2) + 8\alpha^2 R_f K_b(R_f \cos 2\varphi_0 + L_0 \sin\varphi_0)(u - s/2). \quad (14)$$

Defining

$$F_0 = 4\alpha K_t(\varphi_0 - \varphi_i), \quad k_{dt} = 4\alpha^2 K_t \quad (15)$$

which captures the contribution of the torsion spring, and

$$k_{db} = 8\alpha^2 R_f K_b(R_f \cos 2\varphi_0 + L_0 \sin\varphi_0) \quad (16)$$

which represents the contribution of rubber bands, the load-displacement relationship under frictionless conditions simplifies to

$$F = F_0 + (k_{dt} + k_{db})(u - s/2) \quad (17)$$

as illustrated by the dashed line in Fig. 3(b).

B. Distinct Contributions of Torsion Spring and Rubber Bands

The load-displacement relationship in (17) reveals distinct contributions of the torsion spring and rubber bands to the overall system behavior.

The torsion spring produces a resistive force F_0 at $u = s/2$ and a positive dynamic stiffness k_{dt}, both of which are defined in (15). The force F_0 arises from the preload of the torsion spring, as reflected in the term $(\varphi_0 - \varphi_i)$, making it adjustable by selecting torsion springs with different half free angles φ_i. Since both F_0 and k_{dt} are directly proportional to K_t, they can be scaled simultaneously by using torsion springs with different wire and coil diameters. Under the condition where only the torsion spring is engaged, using the parameters in Table I, we obtain $F_0 = 19\,\mathrm{N}$ and $k_{dt} = 3\,\mathrm{N/mm}$, with the corresponding load-displacement curve shown as the dashed line in Fig. 3(c).

In contrast, rubber bands generate zero force at $u = s/2$ but contribute a dynamic stiffness k_{db}, which can be negative, as determined by (16). When $\varphi_0 > 45^\circ$ and L_0 is sufficiently small, the term $(R_f \cos 2\varphi_0 + L_0 \sin\varphi_0)$ becomes negative, leading to $k_{db} < 0$. This implies a negative dynamic stiffness proportional to rubber band stiffness K_b, which can be tuned by adjusting the number of rubber bands. When only the rubber bands are engaged, using the parameters in Table I, we obtain $k_{db} = -5\,\mathrm{N/mm}$, with the corresponding load-displacement curve illustrated by the dashed line in Fig. 3(d).

The resultant force can then be synthesized by superpositioning the effects of the torsion spring and rubber bands, allowing for the tailoring for a high-static-low-dynamic (HSLD) stiffness. The high-static stiffness arises from the torsion spring preload, which increases F_0, while the low-dynamic stiffness k_d is achieved through the negative stiffness k_{db} induced by rubber bands, from geometric nonlinearity. This negative stiffness counteracts the positive stiffness k_{dt} of the torsion spring, resulting in an overall dynamic stiffness given by $k_d = k_{dt} + k_{db}$.

C. Contribution of Friction

The theoretical analysis above assumes frictionless conditions for simplicity; however, in practice, interfacial sliding friction is nonnegligible. To account for this, we derived the contribution of friction through a force equilibrium analysis, detailed in Appendix C, and summarized here for clarity. Friction introduces an additional term to the overall resistive force, given by

$$F - F_{\text{frictionless}} = \mu\left(\iint \alpha R p_{\text{in}} \mathrm{d}S_{\text{in}} + \iint \sqrt{1+\beta}\, p_{\text{out}} \mathrm{d}S_{\text{out}}\right) \quad (18)$$

where μ is the friction coefficient, and $\beta = \alpha^2 R^2 - 2\alpha R \sin\theta_0$. The term $p_{(\cdot)}$ represents contact pressure, and $S_{(\cdot)}$ denotes contact surface area. The subscripts $(\cdot)_{\text{in}}$ and $(\cdot)_{\text{out}}$ correspond to the inner contact surface (between the journal and sleeves) and the outer contact surface (between the bearing and sleeves), respectively.

The contribution of friction is directly related to the contact pressure, resulting in a resistive force that is positive during compression and negative during recovery. This asymmetry induces a hysteresis loop in the load-displacement relationship, shaping the system's behavior during compression and recovery cycles.

D. Compression and Recovery Tests

To validate the theoretical analysis, quasi-static compression and recovery tests were conducted on the knee-inspired hinge prototype using a single-axis MTS material testing machine, with a loading/unloading rate of $0.2\,\mathrm{mm/s}$. The load-displacement curves for both the compression and recovery processes were measured. Each test condition was repeated five times, and the average values along with ± 1 standard deviation are presented in Fig. 3(b)–(d).

As predicted, within the stroke s, the measured results demonstrate a dynamic stiffness roughly consistent with theoretical analysis while also exhibiting a hysteresis loop due to interfacial sliding frictions.

E. Tailorable Mechanical Characteristics

Combining theoretical analyses and experimental results, the load-displacement curve reveals two key characteristics: 1) an HSLD stiffness, which efficiently absorbs energy; and 2) a hysteresis loop, which dissipates energy through friction. To quantitatively evaluate these two properties in relation to impact absorption, we introduce two mechanical characteristics. The first is energy absorption E_a, represented by the purple area under the compression curve in Fig. 3(b), and defined as

$$E_a = \int_0^u F_{\text{compression}} \mathrm{d}u. \quad (19)$$

The second is energy dissipation E_d, indicated by the shaded area between the compression and recovery curves in Fig. 3(b), and defined as

$$E_d = \int_0^u (F_{\text{compression}} - F_{\text{recovery}})\, \mathrm{d}u. \quad (20)$$

To evaluate the efficiency of energy absorption and dissipation, we compare these values against an ideal case where the applied force is constant at F_m, the maximum longitudinal force within

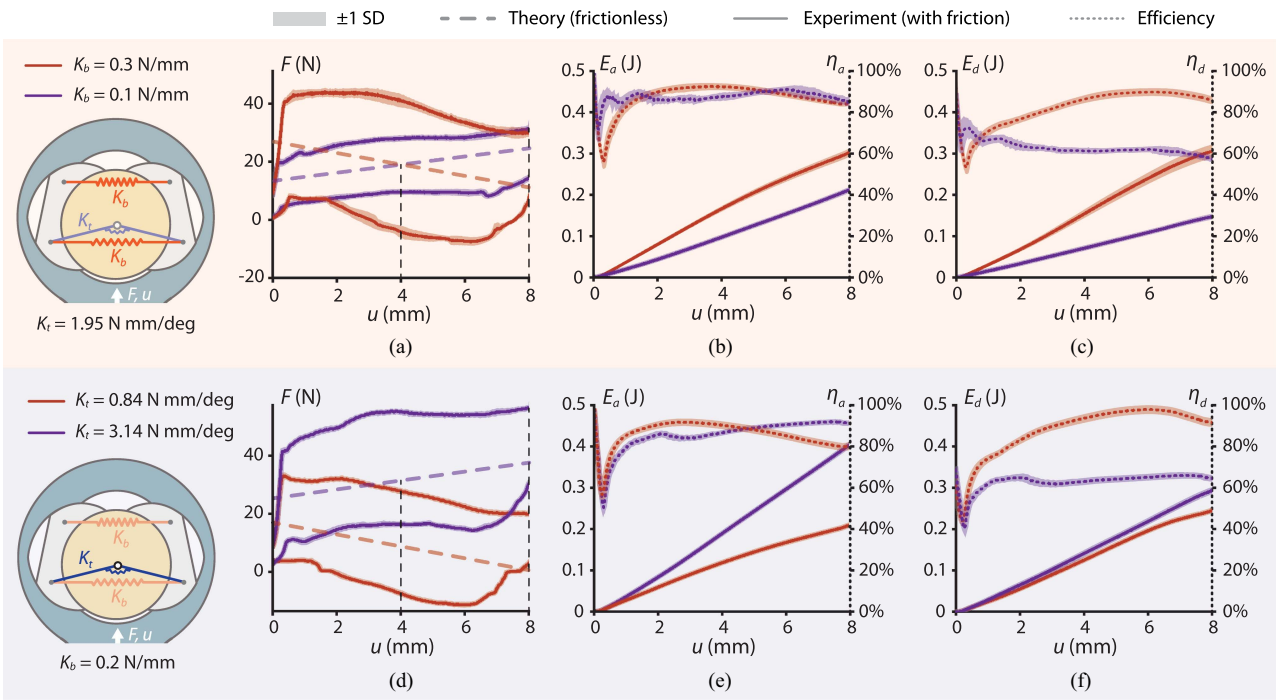

Fig. 4. Force and mechanical characteristics tailored by stiffness of rubber bands and torsion spring. (a)–(c) Force F, energy absorption E_a and its efficiency η_a, and energy dissipation E_d and its efficiency η_d, versus compression u when $K_t = 1.95\,\mathrm{N\,mm/deg}$, reflecting the effects of rubber band stiffness K_b. (d)–(f) Effects of the torsion spring stiffness K_t when $K_b = 0.2\,\mathrm{N/mm}$. Mean measured results of five trials are presented, while surrounding shaded areas indicate ± 1 standard deviation.

the displacement u. The theoretical maximum energy absorption in this ideal case is $E_m = F_m u$. We then define the efficiency metrics for energy absorption and dissipation as

$$\eta_a = E_a/E_m, \quad \eta_d = E_d/E_m. \tag{21}$$

A higher η_a indicates that the joint absorbs the same amount of energy with a lower peak force, while a higher η_d implies that more energy is dissipated rather than rebounded.

As discussed in previous subsections, tuning the stiffness of the torsion spring and rubber bands allows for modification of the $F - u$ curve, thereby tailoring the mechanical characteristics E_a, η_a, E_d, and η_d. This is further confirmed by compression and recovery tests.

1) As shown in Fig. 4(a)–(c), increasing the rubber band stiffness K_b transits the dynamic stiffness from positive to negative, enhancing energy absorption E_a, energy dissipation E_d, and dissipation efficiency η_d, while maintaining η_a at a similar level.
2) As shown in Fig. 4(d)–(f), increasing the torsion spring stiffness K_t transits the dynamic stiffness from negative to positive and increases the force magnitude. This enhances E_a and E_d while keeping η_a at a similar level, but reduces η_d.

The energy absorption efficiency remains high ($\eta_a > 80\%$) across different conditions. Additionally, $F - u$ curves with negative dynamic stiffness exhibit high energy dissipation efficiency ($\eta_d > 80\%$). Based on these features, we select $K_t = 1.95\,\mathrm{N\,mm/deg}$ and $K_b = 0.3\,\mathrm{N/mm}$ for subsequent dynamic experiments and walking demonstrations. This configuration results in a negative dynamic stiffness with a resistive force of approximately $40\,\mathrm{N}$. To apply the knee-inspired hinge in a specific robotic system, the stiffness of the torsion spring and rubber bands can be scaled simultaneously for desired force magnitude (see Appendix D for a demonstration).

F. Effect of Loading Direction

The above analysis discussed the ideal condition where the load aligns with the longitudinal direction along the link connected to bearing; however, in practice, the loading direction may deviate from the longitudinal direction and further affect the load-displacement relationship and corresponding mechanical characteristics in compression and recovery process.

When the longitudinal direction deviates from the loading direction with an angle γ, as shown in Fig. 5(a), the force and displacement along the two directions conform to

$$F_\gamma = F_{\gamma=0}/\cos\gamma, \quad u_\gamma = u_{\gamma=0}\cos\gamma \tag{22}$$

where $(\cdot)_\gamma$ is defined along the loading direction, while $(\cdot)_{\gamma=0}$ is along the longitudinal direction, with the relationship analyzed previously in (17) and (18).

Thereby, the load-displacement relationship under frictionless conditions is

$$F_\gamma = \frac{F_0}{\cos\gamma} + \frac{k_{dt} + k_{db}}{\cos^2\gamma}(u_\gamma - s_\gamma/2) \tag{23}$$

where stroke $s_\gamma = s_{\gamma=0}\cos\gamma$.

Namely, resistive force F_0 at half stroke is magnified by $1/\cos\gamma$, while dynamic stiffness k_d is magnified by $1/\cos^2\gamma$, which slightly decreases the efficiency of energy absorption and dissipation ($< 10\%$ at $\gamma = 30°$), as shown in Fig. 5(b)–(d). As the effect of loading direction is scaled by $1/\cos\gamma \approx 1 + \gamma^2/2$,

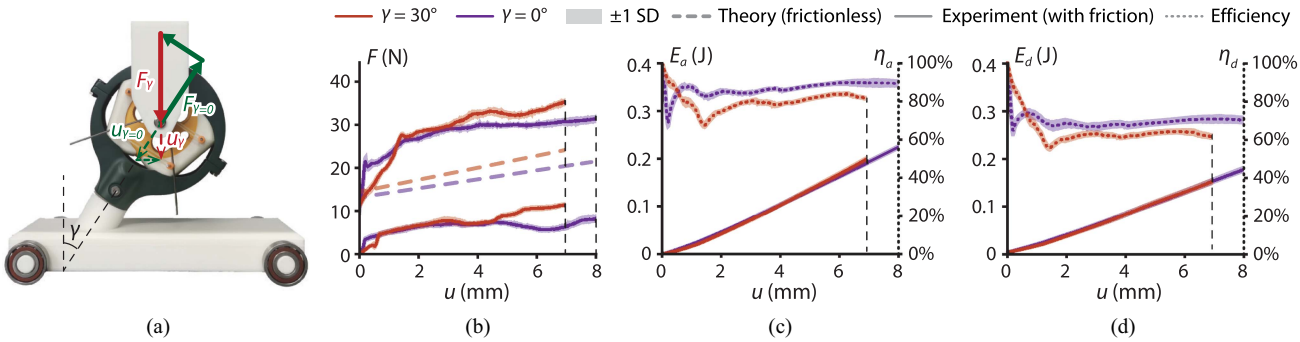

Fig. 5. Force and mechanical characteristics under loading deviating from longitudinal direction. (a) Experimental setup for measuring load-displacement curve with deviation angle γ. (b)–(d) Force F, energy absorption E_a and its efficiency η_a, and energy dissipation E_d and its efficiency η_d, versus compression u when $K_t = 1.75\,\mathrm{N\,mm/deg}$ and $K_b = 0.1\,\mathrm{N/mm}$, reflecting the effects of loading direction indicated by γ. Mean measured results of five trials are presented, while surrounding shaded areas indicate ± 1 standard deviation.

the changes in load-displacement curve and mechanical characteristics are nonsignificant for small deviation angle γ.

In summary, the knee-inspired hinge achieves a load-displacement relationship with HSLD stiffness, which can be programmed by adjusting the stiffness of the torsion spring and rubber bands, enabling highly efficient energy absorption. Additionally, the hysteresis effect caused by interfacial sliding friction also dissipates energy efficiently during the compression and recovery process. The loading deviating from the longitudinal direction slightly reduces energy efficiencies but has little effect for small deviation angle.

IV. Impact Absorption Performance

To evaluate the impact absorption performance of the knee-inspired hinge and analyze its dynamic behavior, we then conducted drop tests and examined the underlying mechanism.

A. Drop Test Setup

In the drop tests, the proposed knee-inspired hinge with a buffer structure serves as the experimental group, using the design parameters listed in Table I. Additionally, two control groups are paralleled for comparison, as illustrated in Fig. 6(a).

1) Silicone pad condition—representing a possible buffering approach using soft materials. In this setup, the entire joint clearance ($s = 8\,\mathrm{mm}$) is filled with a pad made of silicone rubber (Ecoflex 00-10, $E = 55\,\mathrm{kPa}$), which is molded and cured in a 3-D-printed form to fit the available space.
2) No buffer condition—representing the traditional rigid mechanical hinge. Here, the joint clearance is filled with a solid resin block made from the same material as the journal and bearing, effectively eliminating any buffering effect.

For each condition, the joint is released from a fixed height of $H = 8\,\mathrm{mm}$ and allowed to fall freely to hit the ground. The release height is chosen to ensure the maximum acceleration of the distal part upon impacts in no buffer condition within the measurement range of accelerator. To ensure vertical motion, the journal and bearing are connected to two sliders via resin connectors, as shown in Fig. 6(a). A stopper attached to the guide rail limits the uppermost position of the slider connected to the journal, ensuring a consistent release height across three conditions.

To imitate the working conditions of legged robots, where the main body carries most of the weight while being supported by lightweight limbs, an additional payload is attached to the upper part of the joint. As a result, the main body has a weight of $M = 2.52\,\mathrm{kg}$, while the distal part weighs $m = 0.27M = 0.68\,\mathrm{kg}$.

Two synchronized inertial measurement units (IMUs) (MTi-300, Xsens) are mounted on the main body and distal part to measure the vertical accelerations at 2000 Hz. These measurements are used to analyze the joint kinematics and interaction forces during impact events. Body velocity and joint compression are computed by trapezoidal numerical integration of the acceleration data over time. The ground reaction force (GRF) is estimated by combining acceleration and mass information. Each test condition is repeated five times to ensure repeatability and statistical reliability.

B. Enhanced Impact Absorption in Drop Tests

For all three buffering conditions, the system can be approximated using a two-mass model, as illustrated in Fig. 6(b). Upon ground impact with an initial velocity of $v_0 = 0.21\,\mathrm{m/s}$, the main body then decelerates under the combined effect of the joint interaction force F_j and gravitational force Mg, eventually coming to rest at maximum compression $u_{\max}$, as shown in Fig. 6(c)–(d). The peak acceleration of the main body occurs during this deceleration phase.

Fig. 6(e) compares body acceleration across three conditions. While silicone pad, a conventional soft buffering material, reduces the peak body acceleration by 48% than the rigid hinge with no buffer, our knee-inspired hinge with buffer structure further reduces the acceleration by 62% compared to the silicone-buffered hinge. This results in an overall 80% reduction in peak body acceleration compared to the rigid hinge.

Given that the main body is significantly heavier than the distal part, the reduced body acceleration translates into a substantial decrease in ground impact force. The GRF is given by $F_g = Ma_b + ma_d + (M + m)g$, where g is the gravitational acceleration. Consequently, while the silicone pad reduces peak

IEEE Transactions on Robotics (T-RO) paper, presented at ICRA 2026, Vienna, Austria. Cite as T-RO paper.

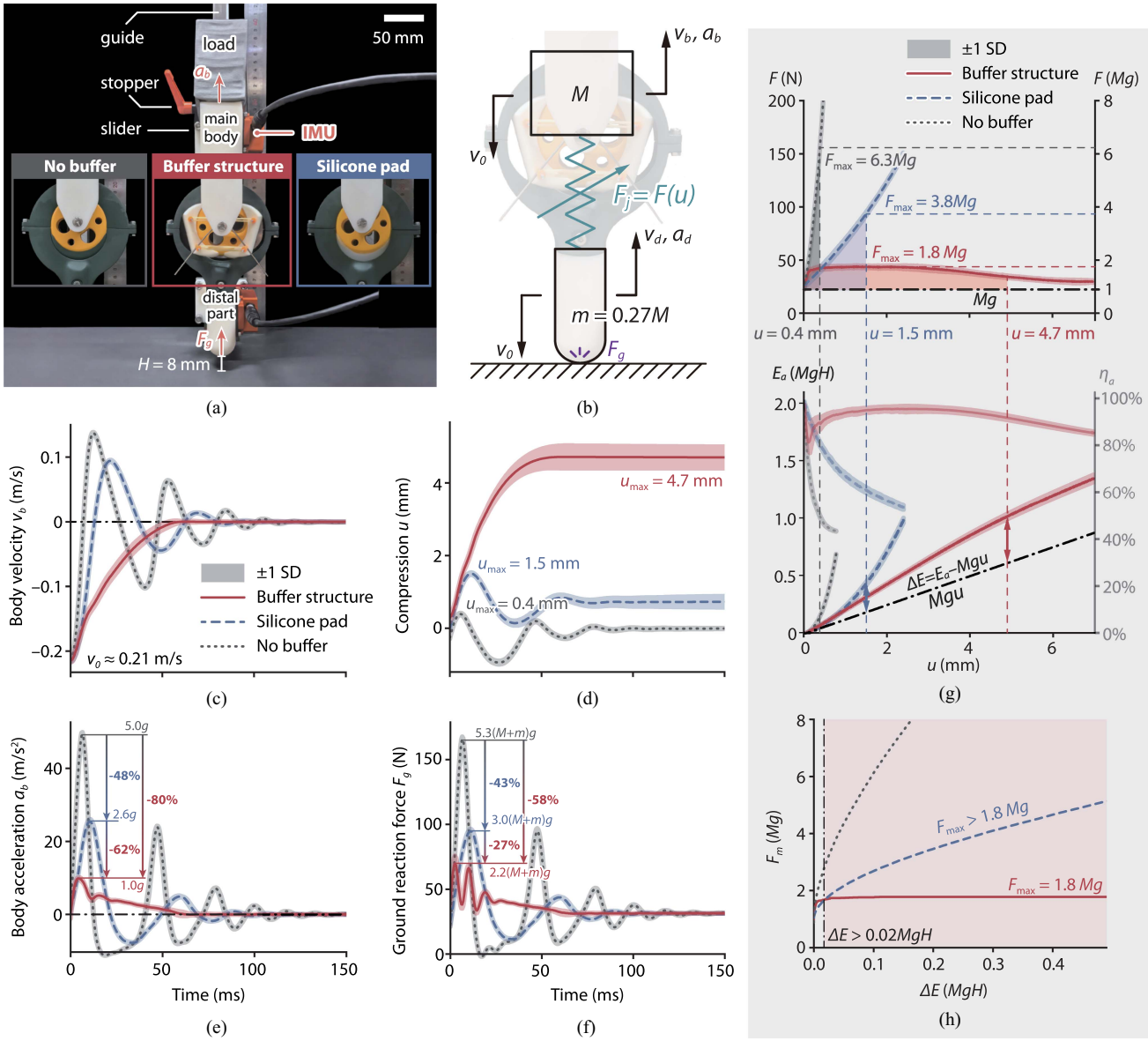

Fig. 6. Impact absorption performance of the knee-inspired hinge compared with silicone pad and no buffer conditions. (a) Drop tests setup, experiment group, and control groups. (b) Model of joints under impact. (c)–(f) Body velocity, compression, body acceleration, and GRF versus time, compared across three conditions. Mean measured results of five trials are presented, with shaded areas indicating ±1 standard deviation. (g) Load-displacement curve and energy absorption characteristics of the three conditions. The shaded area between the compression curve and Mg indicates the kinetic energy absorbed by the joint. Shallow lines indicate energy absorption efficiency η_a. (h) Maximum joint force F_m versus kinetic energy absorption ΔE. Shaded area indicates the range where the knee-inspired hinge outperforms the silicone pad.

GRF by 43% compared to the rigid hinge, the knee-inspired hinge further reduces GRF by 27% relative to the silicone-buffered hinge, leading to a total 58% reduction from the rigid hinge, as shown in Fig. 6(f).

These substantial reductions in body acceleration and GRF confirm the superior impact absorption performance of the knee-inspired hinge.

C. Underlying Mechanism of Enhanced Impact Absorption

The difference in impact absorption performance across three conditions stems from the distinct load-displacement relationships and corresponding mechanical characteristics of the joints, as shown in Fig. 6(g). Intuitively, the two control groups exhibit similar J-shaped $F-u$ curves with different stiffness, while that of the knee-inspired hinge has a completely different shape with HSLD stiffness, resulting in a significantly higher energy absorption efficiency η_a.

Upon impact, the initial kinetic energy of the main body is primarily absorbed through the negative work done by the resultant force of joint resistance and gravity (see Appendix E for details), expressed as

$$\frac{1}{2}Mv_0^2 \approx \int_0^{u_{\max}} (F_j - Mg)\mathrm{d}u = E_a - Mgu \triangleq \Delta E. \quad (24)$$

Therefore, absorbing a given amount of energy ΔE, indicated by the shaded areas in Fig. 6(g), the knee-inspired hinge has lower peak force ($1.8\,Mg$) than silicone pad buffer ($3.8Mg$),

due to its load-displacement curve with HSLD stiffness and high η_a. This constrained joint force further leads to the reduction in body acceleration, as $a_b = F_j/M - g$. The peak accelerations measured in drop tests are roughly consistent with the maximum joint force in $F-u$ curves within the maximum compression $u_{\max}$.

Moreover, when considering the maximum joint force required for a given amount of kinetic energy absorption, the knee-inspired hinge confines the peak force below $1.8Mg$ regardless of increasing energy ΔE, owing to its negative dynamic stiffness. In contrast, the maximum force $F_{\max}$ in the silicone pad condition increases with ΔE, as illustrated in Fig. 6(h). Consequently, for a wide range of kinetic energy absorption ($\Delta E > 0.02\,MgH$), the knee-inspired hinge maintains a lower joint force, with the reduction rate rising as ΔE increases.

In summary, by efficiently absorbing kinetic energy while confining the joint force, our knee-inspired hinge outperforms conventional soft-materials buffering methods. It effectively mitigates body acceleration, enhancing protection for the robot body, and significantly reduces GRF under impacts, thus ensuring safer interaction with the surrounding environment.

V. Enhancement of Interaction Safety in a Demonstration Walking Robot

To demonstrate the application of our knee-inspired hinge in legged robots for enhancing interaction safety, we developed a single-actuated biped robot and conducted untethered walking experiments to compare its impact absorption performance.

A. Single-Actuated Biped Walking Robot

The structure of the biped walking robot is shown in Fig. 7(a). It features a single degree-of-freedom (DOF) actuation, driven by a motor fixed to the body frame. For simplification, its walking mechanism can be described as planar motion in the sagittal plane, as illustrated in Fig. 7(b).

The key component of the robot is an inverted slider-crank mechanism, which converts the motor's monotonic rotation into periodic leg swinging while ensuring foot clearance. Taking the right side as an example, an eccentric wheel with center H, attached to the end of the motor shaft at O, acts as the crank OH, driven counterclockwise relative to the body frame OS by the motor. The crank length $|OH|$ thus corresponds to the eccentricity e. Additionally, the eccentric wheel also serves as the journal of the hinge, constraining the robot leg, connected to the bearing, to rotate about the journal center H. The leg also passes through a slider that is linked to a rolling bearing fixed on the body frame, allowing it to rotate solely about S. As a result, leg orientation is determined by its collinearity with HS, which depends on motor angle ψ, given the body length $|OS| = h$. For ground contact, a flat foot with length L_f is rigidly fixed to the end of the robot leg, ensuring a stable stance. Additionally, cylindrical rods of length w_f, acting as heel and toe supports, are fixed at points P_H and P_T, respectively, providing lateral stability during stance. The leg length L is defined as the distance from H to the flat foot when the joint is uncompressed.

TABLE II
Parameter of Single-Actuated Biped Robot

Parameter	Value	Unit
Eccentricity e	15	mm
Body length h	110	mm
Leg length L	357	mm
Foot length L_f	155	mm
Toe/Heel length w_f	125	mm
Weight of main body M_r	3.2	kg
Weight of leg and foot m_r	0.5	kg
Motor speed ω	10	rpm
Step period $T/2$	3	s

The contralateral leg adopts the same architecture but with the crank OH' oriented in the opposite direction to OH. Therefore, by actuating both cranks OH and OH' with a single motor rotating at a constant speed $\dot{\psi} = \omega$, the two legs undergo reciprocal sweeping motion relative to the body, maintaining opposite phase and equal period $T = 2\pi/\omega$. The mechanism ensures a foot clearance of $2e$ at midstance, when $\psi = n\pi$ ($n \in \mathbb{Z}$), where HS and $H'S$ become collinear.

A prototype of the untethered single-actuated biped walking robot was developed using the parameters listed in Table II. The body frame, hollow robot legs, and feet are fabricated from aluminum alloy, while the heels and toes are made of cylindrical steel bars. A 3-D-printed resin connector is attached to the body frame to support the power, control, and measurement systems. The robot is actuated by a motor (HOLLOW 10025, AcmeMach), which is hollow, allowing a two-ended crankshaft to pass through and drive both cranks simultaneously. The motor is powered by two Li-ion batteries (Grepow, 1800 mAh, 4S), positioned symmetrically for fore-aft balance, and controlled via a PID controller implemented on an STM32 microcontroller to maintain a constant rotation speed.

With constant motor rotation, the biped robot achieves a walking gait with a step period of 3 s. Each step cycle consists of three distinct phases—weight acceptance, wobbling stance, and steady stance, as shown in Fig. 7(c). At first, the flat foot of the contralateral leg provides stable support until the heel of the swinging leg contacts the ground, initiating a new step cycle. Then, the weight transfers to the stance leg, while the robot rolls forward pivoting on the heel until the toe strikes the ground, completing the weight acceptance phase. The toe-strike impact then induces back-and-forth oscillation, where the robot pivots alternately on the toe and heel. It is named as wobbling stance phase, until the vibration is finally mitigated and the stance foot contacts the ground steadily. Once oscillations subside, it enters the steady stance phase, where the stance foot maintains stable ground contact until the contralateral heel touches ground, initiating the next step cycle.

B. Walking Experiment Setup

To characterize the kinematics and dynamics of the walking process, synchronized measurements were adopted, as illustrated in Fig. 7(a). The positions of heels, toes, and journal

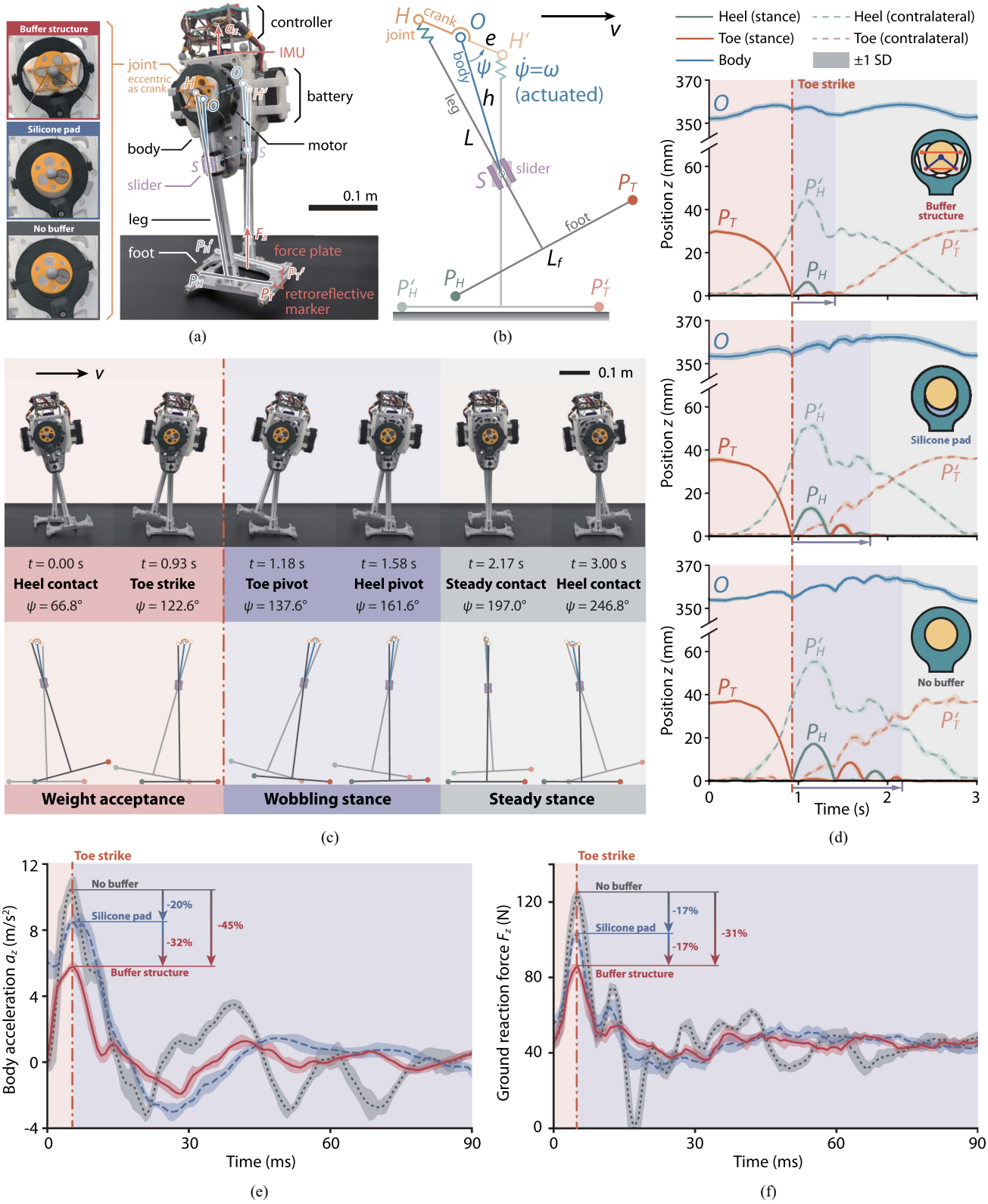

Fig. 7. Application of the knee-inspired hinge in a demonstration single-actuated biped walking robot. (a) Prototype of single-actuated biped walking robot and experimental setup. (b) Inverted slider-crank mechanism modeling the biped walking actuated by a motor rotating at a constant speed. (c) Walking sequence over a step, with the dark lines and symbols indicating the stance side, and the shallow ones indicating the contralateral side. (d) Vertical positions of heel, toe, and body versus time over a step. (e)–(f) Vertical body acceleration and GRF versus time around toe-strike. Mean measured results of five trials are presented, with surrounding shaded areas indicating ±1 standard deviation.

centers were tracked using eight motion capture cameras (Vicon), which captured retroreflective markers attached to key points at a sampling rate of 200 Hz. The body position was represented by the midpoint of journal centers. The body acceleration was measured using a wireless IMU (Blue Tradient, Vicon), sampling at 1200 Hz. The resultant GRF from both legs was recorded by the underfoot force plate (Bertec), sampling at 1000 Hz.

Similar to the drop test setup, the impact absorption performance of the knee-inspired hinge was compared with two control groups—silicone pad buffering condition, and no buffer condition, by substituting the joint connecting robot leg and motor shaft, as shown in Fig. 7(a). Five trials are repeated for each working condition.

C. Enhanced Impact Absorption in Walking Experiments

During walking, impacts occur at toe-strike, leading to a sharp increase in body acceleration and GRF, followed by subsequent wobbling. A clear difference across the three joint conditions is the progressive reduction in the duration of the wobbling stance phase, from the no buffer condition to the silicone pad condition to the knee-inspired hinge, as shown in Fig. 7(d). The reduction in body acceleration and GRF are also significant. While silicone pad reduces the peak body acceleration by 20% than the rigid hinges, our knee-inspired hinge further reduces the acceleration by 32% compared to the silicone buffered hinge, which means a reduction of 45% from the rigid one, as shown in Fig. 7(e). Similarly, while silicone pad reduces the peak GRF by 17% than the rigid hinges, our knee-inspired hinge further reduces the acceleration by 17% compared to the silicone buffered hinge, which means a reduction of 31% from the rigid one, as shown in Fig. 7(f). These reductions in wobbling phase duration, body acceleration, and GRF confirm the enhanced impact absorption of our knee-inspired hinge.

In summary, the biped walking robot based on inverted slider-crank mechanism demonstrates the application of our knee-inspired hinge in robots, and its outperformance over buffer methods of soft materials. The periodic impacts with the ground are absorbed by the knee-inspired hinge, thus mitigating induced vibration to improve stability, confining body acceleration for robot protection, and reducing GRF for the safety of the surrounding environment.

VI. Conclusion

The proposed knee-inspired hinges modified traditional revolute joints by incorporating a buffer structure between the journal and the bearing to absorb longitudinal impacts along articulated links, thus providing a compact solution for enhancing robot-environment interaction safety. Inspired by the architecture of human knees, the buffer structure consisted of a pair of rigid C-shaped sleeves linked to elastic components. Under compression, these sleeves rotated upwards, loading elastic elements to generate resistance, which included torsion springs and rubber bands providing positive and negative stiffness to the load-displacement relationship, respectively. By tuning these components, the load-displacement relationship can be programmed, for example, to achieve an HSLD stiffness for greater energy absorption efficiency. This force characteristic not only confined the acceleration propagated to the main body, protecting the robot, but also reduced the interaction force with the environment, safeguarding the surroundings, as validated by drop tests and walking experiments.

To the best of our knowledge, our knee-inspired hinge was the first revolute joint that integrated the longitudinal impact absorption function and can be easily applied in robotic systems by replacing the mechanical hinges directly. The effectiveness and practicality of the design were demonstrated in a biped walking robot. Beyond legged robots, this hinge has promising potential for human-centered applications as well, such as exoskeletons and prostheses. Even in bionic joints adopting four-bar linkage to fit the moving rotation axis of knee in these working conditions [54], [55], our hinge is still available by replacing the hinges in the linkage for impact absorption.

The ease of application for our hinges stems from the design paradigm of “understanding-to-building”. Rather than merely replicating the complex structure of human knees, we abstracted the underlying mechanism and adapted it into the modified structure for an elastic longitudinal movement along articulated link in mechanical hinges. This single function of longitudinal impact absorption is an initial step in practicing the design paradigm. In future work, the multifunctionality of biological joints is reasonably expected to be engineered in mechanical hinges, with longitudinal compliance incorporated with rotational compliance [53], actuation [56], and variable stiffness [43] in a single bioinspired hinge, which may further affect the control for locomotion and enhance its performance in physical robot-environment interaction. In addition to physical interaction safety, the energy absorption feature of the knee-inspired hinge may also pave the way for noise reduction, which is worth further investigation to accelerate seamless integration of robots into human society.

Appendix

A. Stiffness Against Axial Force and Radial Moment Load

In the geometric design of the knee-inspired hinge, an elliptical profile is adopted in the radial sections to confine the relative movement as planar motion and thus strengthen the hinge stability against axial force and radial moment load. To further strengthen this stiffness, knee-inspired hinges can be mounted in pairs to support the shaft on two ends.

To quantify the stiffness of the knee-inspired hinge and the paired configuration against axial force and radial moment load, compression tests were conducted with a single-axis MTS testing machine measuring the displacements under axial force and radial moment load. Control groups of rigid mechanical hinge without buffer and silicone pad buffered hinge, with journal and bearing adopting the same elliptical radial section and made from the same material as that of the knee-inspired hinge, are paralleled for comparison, as shown in Fig. 8(a).

In the axial force loading experiment, the bearing was fixed to the ground, while the force was exerted at the center of the journal, with experimental setup and results shown in Fig. 8(b).

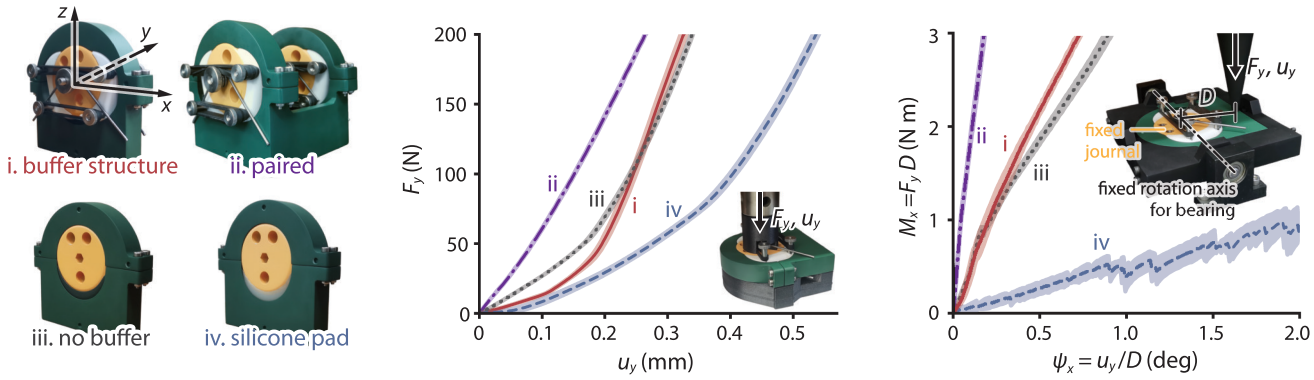

(a) (b) (c)

Fig. 8. Stiffness against axial force and radial moment load. (a) Experiment and control group. (b) Axial force F_y versus displacement u_y. (c) Radial moment M_x versus angular displacement ψ_x. Mean measured results of five trials are presented, while surrounding shaded areas indicate ± 1 standard deviation.

TABLE III
STIFFNESS AGAINST AXIAL FORCE AND RADIAL MOMENT LOAD

Stiffness against	axial force	radial moment
Paired	757	22.1
Buffer structure	614	4.9
No buffer	590	4.6
Silicone pad	373	0.5
Unit	$\mathrm{N/mm}$	$\mathrm{N\,m/deg}$

The stiffness evaluated for $F_y = 200\,\mathrm{N}$ is also compared in Table III, showing that the axial stiffness of knee-inspired hinge is comparable to rigid mechanical hinge ($\approx 600\,\mathrm{N/mm}$), while mounting them in pairs strengthen it to $757\,\mathrm{N/mm}$ and silicone pad buffer method weaken it to $373\,\mathrm{N/mm}$.

In the radial moment loading experiment, the journal is fixed, while the bearing is restricted to rotate about a fixed axis crossing the journal center. Thus, exerting a force F_y at the point deviating from the journal center with distance $D = 60\,\mathrm{mm}$ is equivalent to a radial moment load of $M_x = FD$, and the induced angular displacement can be calculated as $\psi_x = u_y/D$. Experimental setup and results are shown in Fig. 8(c). The stiffness evaluated for $M_x = 1\,\mathrm{N\,m}$ is also compared in Table III, showing that the stiffness against radial moment of knee-inspired hinge is comparable to rigid mechanical hinge ($4.6 - 4.9\,\mathrm{N\,m/deg}$), while mounting them in pairs strengthen it about 4.5 times to $22.1\,\mathrm{N\,m/deg}$ and silicone pad buffer method weaken it to $0.5\,\mathrm{N\,m/deg}$.

In summary, the stiffness against axial force and radial moment load in the knee-inspired hinge is comparable to that in rigid mechanical hinge, which is higher than the silicone pad buffered condition, showing better hinge stability. Moreover, mounting the hinges in pairs can further strengthen these stiffness significantly for possible application requirement.

B. Selection of Geometry Parameter

The size of the knee-inspired hinge can be adjusted according to the application requirements. Only the proportion constant α needs to be carefully selected.

When α increases, the sleeve profile gets closer to the journal, as shown in Fig. 9(a), which means the C-shaped sleeves take less space, thus reducing joint size. However, increasing α in the sleeve profile will raise a new issue. When deriving the expression of $r(\theta)$, we adopt the hypothesis that Δu and $\Delta\varphi$ are minims, which is the foundation of linearization reserving only the small quantity of first order. Therefore, with increased Δu forcing the C-shaped sleeves to slide relative to the bearing, there will be errors between the bearing profile and the sleeve profile after combined rotation and translation, as illustrated in Fig. 9(b) with an example of amplified $\Delta u = 12\,\mathrm{mm}$ to make the errors obvious. In the prototype, Δu is limited within $[-4,\ 4]$ mm.

Defining the error as the vertical distance from bearing to sleeve, where the sleeve has an angular length of $40°$, we can find the effects of α on the maximum error $err_{\max}$, as shown in Fig. 9(c). For negative Δu, the error is less affected by α, always smaller than 0.2 mm. For positive Δu, the error increases with Δu and α.

Thus, increasing α is double-edged—it saves joint space, but increases the error from conformal condition. Here, we select a compromise $\alpha = 3.35°/\mathrm{mm}$, restricting the error below 0.2 mm, consistent with the accuracy of manufacture.

C. Force Equilibrium Analysis Considering Frictions

Load-displacement relationship under frictionless conditions can be obtained with virtual work principle. However, compression and recovery tests show nonnegligible effects of frictions. Here, we will demonstrate the role of interfacial frictions by force equilibrium analysis, with the bottom right of the system as an example without loss of generality.

As the profile of the contact surface is important to derive the tangential direction, aligning with the friction, we need to provide the expression of $r_{\Delta\varphi}(\theta)$ at first, which represents the contact line between the C-shaped sleeve and bearing in the sagittal plane when the sleeve rotates an angle $\Delta\varphi$ about journal axis O relative to φ_0, and can be written as

$$r_{\Delta\varphi}(\theta) = \frac{1}{\alpha}\left[\sin(\theta - \Delta\varphi) + \sqrt{\sin^2(\theta - \Delta\varphi) + \beta}\right] \quad (25)$$

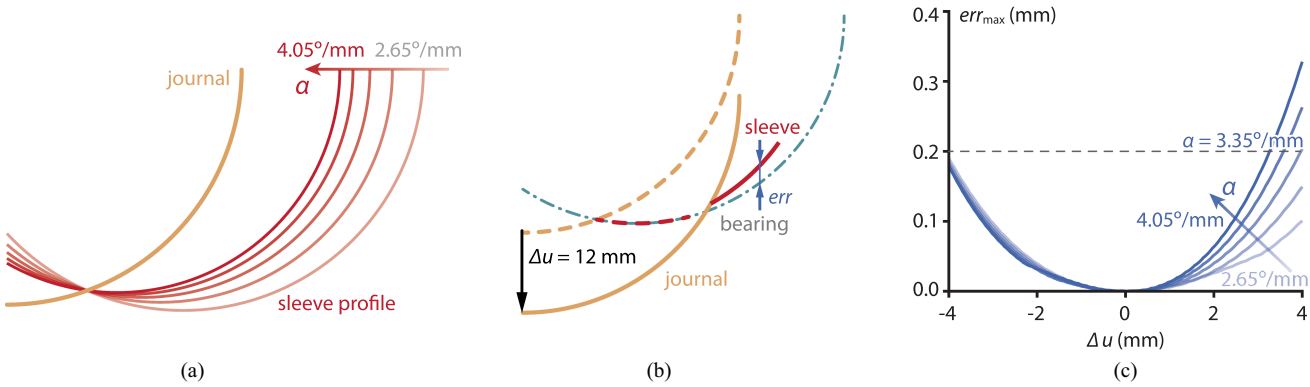

(a) (b) (c)

Fig. 9. Effects of proportion constant α. (a) Sleeve profile with α ranging from $2.65°/\text{mm}$ to $4.05°/\text{mm}$ in an interval of $0.35°/\text{mm}$, indicated by lines from shallow to dark. (b) Definition of profile error from the exact conformal condition, exampled for $\Delta u = 12\,\text{mm}$ to make the errors obvious. (c) Maximum error $err_{\max}$ versus Δu curves for different α.

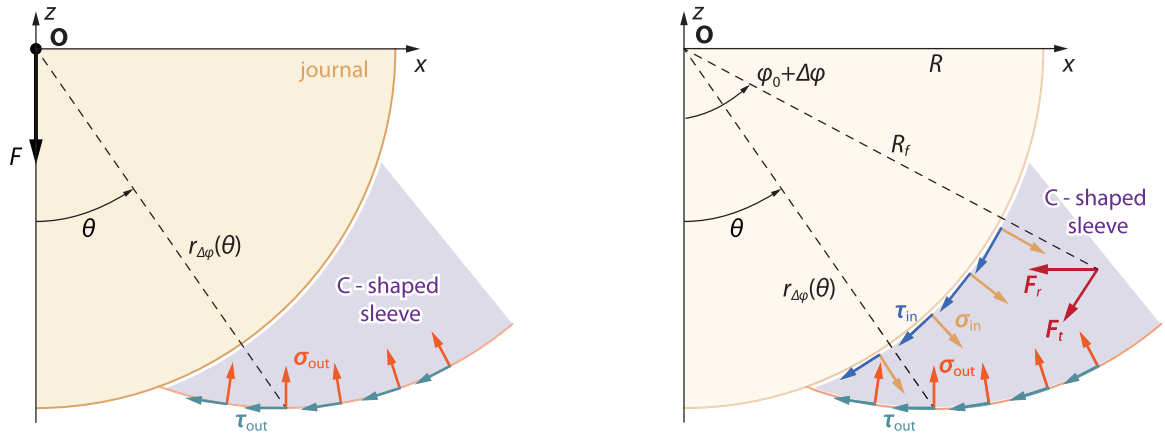

(a) (b)

Fig. 10. Force analysis. (a) External forces exerted on the system composed of journal and C-shaped sleeve in a sagittal section. (b) Forces exerted on the C-shaped sleeve in the sagittal section.

where β represents a function of R as

$$\begin{aligned}\beta &= \alpha^2 R^2 - 2\alpha R \sin\theta_0 \\ &= \alpha^2 r_{\Delta\varphi}^2(\theta) + 2\alpha r_{\Delta\varphi}(\theta)\sin(\theta - \Delta\varphi)\end{aligned} \tag{26}$$

varying across different sagittal sections.

The derivative of $r_{\Delta\varphi}(\theta)$ respective to θ is

$$r'_{\Delta\varphi}(\theta) = \frac{r_{\Delta\varphi}(\theta)\cos(\theta - \Delta\varphi)}{\alpha r_{\Delta\varphi}(\theta) - \sin(\theta - \Delta\varphi)}. \tag{27}$$

Expressing the outer contact line (between the bearing and sleeve) in Cartesian coordinate system as $x = r_{\Delta\varphi}(\theta)\sin\theta$, $z = -r_{\Delta\varphi}(\theta)\cos\theta$, the tangential direction $\boldsymbol{t}_{\text{out}}(\theta) \parallel (\mathrm{d}x/\mathrm{d}\theta,\ \mathrm{d}z/\mathrm{d}\theta)^{\intercal}$ is

$$\boldsymbol{t}_{\text{out}}(\theta) = -\frac{1}{\sqrt{1+\beta}}\begin{bmatrix}\alpha r_{\Delta\varphi}(\theta)\cos\theta + \sin\Delta\varphi \\ \alpha r_{\Delta\varphi}(\theta)\sin\theta - \cos\Delta\varphi\end{bmatrix} \tag{28}$$

and the normal direction $\boldsymbol{n}_{\text{out}}(\theta) \perp \boldsymbol{t}_{\text{out}}(\theta)$ is

$$\boldsymbol{n}_{\text{out}}(\theta) = \frac{1}{\sqrt{1+\beta}}\begin{bmatrix}-(\alpha r_{\Delta\varphi}(\theta)\sin\theta - \cos\Delta\varphi) \\ \alpha r_{\Delta\varphi}(\theta)\cos\theta + \sin\Delta\varphi\end{bmatrix}. \tag{29}$$

Thereby, analyzing the external forces exerted on the system composed of journal and C-shaped sleeve, as shown in Fig. 10(a), the longitudinal force F is balanced by distributed friction $\boldsymbol{\tau}_{\text{out}}$ aligning with $\boldsymbol{t}_{\text{out}}(\theta)$, and in-plane components of pressure $\boldsymbol{\sigma}_{\text{out}}$ aligning with $\boldsymbol{n}_{\text{out}}(\theta)$ at the contact surface between the C-shaped sleeve and bearing.

Taking the compression process as an example, the vertical force equilibrium finds

$$\begin{aligned}F = &\iint \frac{1}{\sqrt{1+\beta}}\sigma_{\text{out}}[\alpha r_{\Delta\varphi}(\theta)\cos\theta + \sin\Delta\varphi]\mathrm{d}S_{\text{out}} \\ &- \iint \frac{\mu}{\sqrt{1+\beta}}p_{\text{out}}[\alpha r_{\Delta\varphi}(\theta)\sin\theta - \cos\Delta\varphi]\mathrm{d}S_{\text{out}}\end{aligned} \tag{30}$$

where p_{out} and S_{out} are the spatial pressure and area of the outer contact surface. μ is the friction coefficient.

Then, analyzing the moment equilibrium of the C-shaped sleeve about O, which is subject to pressure and friction along two contact surfaces, and forces from rubber bands F_r and torsion spring F_s, as shown in Fig. 10(b), we have

$$F_r R_f \cos(\varphi_0 + \Delta\varphi) + F_s R_f + \mu \iint R p_{\text{in}}\mathrm{d}S_{\text{in}}$$

IEEE Transactions on Robotics (T-RO) paper, presented at ICRA 2026, Vienna, Austria. Cite as T-RO paper.

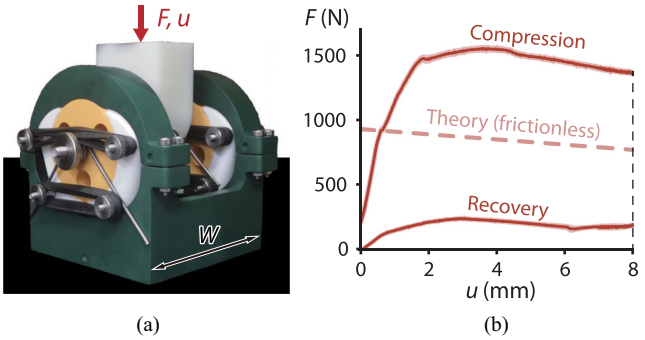

Fig. 11. Example of modified knee-inspired hinge for a leg prosthesis. (a) Prototype for compression and recovery tests. (b) Force-displacement curve tailored for application in prosthesis. Mean measured results of five trials are presented, while surrounding shaded areas indicate ±1 standard deviation.

$$= \iint \frac{1}{\sqrt{1+\beta}} \sigma_{\text{out}} r_{\Delta\varphi}(\theta) \cos(\theta - \Delta\varphi) \mathrm{d}S_{\text{out}}$$
$$- \iint \frac{\mu r_{\Delta\varphi}(\theta)}{\sqrt{1+\beta}} p_{\text{out}} [\alpha r_{\Delta\varphi}(\theta) - \sin(\theta - \Delta\varphi)] \mathrm{d}S_{\text{out}} \quad (31)$$

where p_{in} and S_{in} are the spatial pressure and area of the inner contact surface (between the journal and sleeve).

Neglecting the minim of high order and combining (30) and (31), there is

$$F = \alpha [F_r R_f \cos(\varphi_0 + \Delta\varphi) + F_s R_f] + \mu \left(\iint \alpha R p_{\text{in}} \mathrm{d}S_{\text{in}} + \iint \sqrt{1+\beta} p_{\text{out}} \mathrm{d}S_{\text{out}} \right) \quad (32)$$

where the first two terms reflect the contribution of rubber bands and torsion spring, consistent with the frictionless condition. The latter two terms reflect the contribution of frictions at the inner and outer contact surface, positively correlated to the contact pressure. The friction term is positive in compression, and negative in recovery, thereby synthesizing the hysteresis load-displacement in compression and recovery tests.

D. Modification for Specific Robotic System

To apply our concept of knee-inspired hinge in diverse robotic systems, modifications may be needed to satisfy specific force requirements.

Taking leg prosthesis for an 80 kg person as an example, knee-inspired hinges can be mounted in pairs, as shown in Fig. 11(a), to strengthen joint stability and halve the required longitudinal resistant force of a single hinge. The lateral width of the whole joint is set as $W = 100\,\text{mm}$, referring to the size of human knee joints [57].

Then the longitudinal force of the joint should be tailored according to the body weight. Referring to the maximum leg force during human running, the longitudinal joint force in leg prosthesis is expected to be limited within twice the body weight, that is, $2 \times 80 \times 9.8 = 1,568\,\text{N}$. To achieve this goal, the stiffness of the torsion spring and rubber bands are scaled simultaneously to magnify the joint resistant force while maintaining the negative dynamic stiffness. The free angle of the torsion spring is also reduced to increase the force magnitude.

Adopting torsion springs of $18.3\,\text{N mm/deg}$ and rubber bands of $1.0\,\text{N/mm}$ (9.4 and 3.3 times of joints with maximum force as $40\,\text{N}$, respectively), there is $K_t = 4 \times 18.3 = 73.2\,\text{N mm/deg}$ and $K_b = 4 \times 1.0 = 4.0\,\text{N/mm}$ for the total joint with hinges mounted in pairs and elastic elements arranged on both sides. The free angle of the torsion spring is also reduced to 30° from original 45°. The resulting force-displacement curve is shown in Fig. 11(b), with a maximum force of $1,560\,\text{N}$ and negative dynamic stiffness $k_d \approx -20\,\text{N/mm}$, fitting the force requirement of leg prosthesis.

E. Impact Dynamics From the View of Energy Absorption

To explain the different joint performances across three conditions in drop tests with the measured $F - u$ curves, we analyze the dynamic impact process from the view of energy absorption.

The main body is only subject to gravity Mg and joint interaction force F_j, as shown in Fig. 6(b). Thereby, the governing equation is

$$M\dot{v}_b = F_j - Mg \quad (33)$$

which can also be written as

$$M\dot{v}_b v_b = (F_j - Mg)v_b = (F_j - Mg)(-\dot{u} + v_d) \quad (34)$$

where M is the body mass. v_b and v_d are velocities of the main body and distal part, respectively. $\dot{u}$ is the compression rate, defined as $\dot{u} = v_d - v_b$.

Integrating the equation with time, there is

$$\frac{1}{2}Mv_b^2 - \frac{1}{2}Mv_0^2 = \int (F_j - Mg)\mathrm{d}z_d - \int (F_j - Mg)\mathrm{d}u \quad (35)$$

where v_0 is the initial velocity immediately before impact.

As the contact stiffness between the rigid distal part and ground is much higher than the joint stiffness in knee-inspired joint and silicone pad condition, z_d is much smaller than u, where the latter is dominated by z_b. Therefore, (35) can be approximated as

$$\frac{1}{2}Mv_0^2 - \frac{1}{2}Mv_b^2 \approx \int_0^u (F_j - Mg)\mathrm{d}u. \quad (36)$$

The underlying physical meaning is that the kinetic energy of the main body is mainly absorbed with the negative work done by the resultant force of joint resistance and gravity. Thereby, the dynamic performance under impact can be predicted by the measured load-displacement curves of joints.

Particularly, when the main body velocity is reduced to 0, the initial kinetic energy of the main body immediately before impact is all absorbed by the joint, with the compression reaching its maximum value $u_{\max}$, i.e.,

$$\frac{1}{2}Mv_0^2 \approx \int_0^{u_{\max}} (F_j - Mg)\mathrm{d}u. \quad (37)$$

To validate the dynamic analysis above, we then simulate the body acceleration with (36) and compare it with the results of drop tests across three joint conditions.

The governing equation can be written as

$$M\ddot{u} = F_j - Mg \quad (38)$$

equivalent to (36) as the compression is dominated by the displacement of the main body.

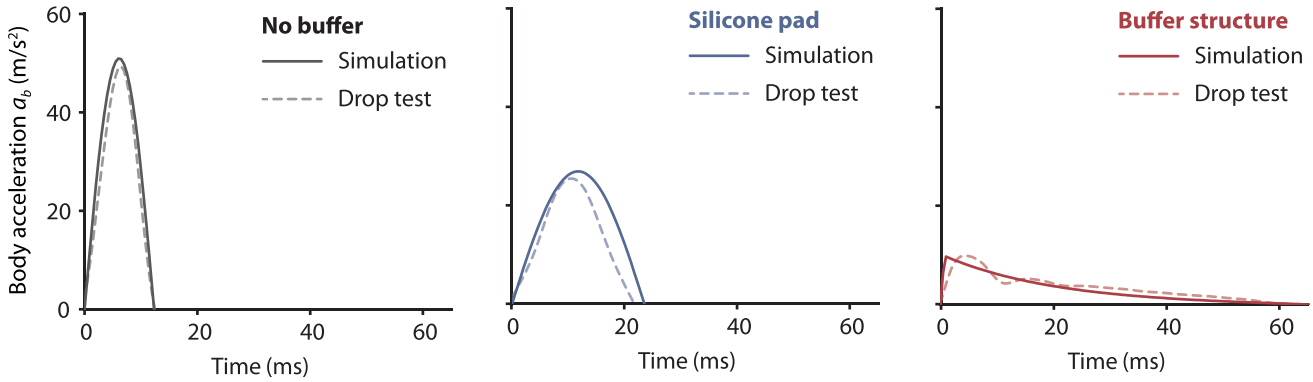

Fig. 12. Simulation results with simplified model. Body acceleration versus time under impacts in three joint conditions, with simulation results roughly matching the drop tests. Solid lines indicate simulation results, and shallow dashed lines indicate measured results from drop tests.

Therefore, the dynamic response is determined by the resultant force $F_j - Mg$ curve versus compression u. For simplicity, the load-displacement relationships of the joints with no buffer condition or silicone pad condition are modeled as linear, i.e., $F_j - Mg = ku$, with stiffness taken as $k = 164\,\mathrm{N/mm}$ and $k = 45\,\mathrm{N/mm}$, respectively. Similarly, the resultant load-displacement curve of knee-inspired joint is simplified as piecewise linear. At first, the joint force grows with $k = 164\,\mathrm{N/mm}$, same as the no buffer condition, until it reaches a criterion F_i. Then the dynamic negative stiffness turns to be negative as $k_d = -6\,\mathrm{N/mm}$, i.e.,

$$F_j - Mg = \begin{cases} ku, & 0 \le u \le F_i/k \\ F_i + k_d(u - F_i/k), & u > F_i/k \end{cases} \tag{39}$$

where F_i is here taken as Mg to fit the force characteristics of the knee-inspired joint in drop tests.

As the maximum acceleration of the main body appears at its first peak, we simulate the first half cycle with MATLAB ode45, with mass $M = 2.52\,\mathrm{kg}$ and $v_0 = 0.21\,\mathrm{m/s}$, consistent of drop tests.

Simulation results roughly match the experimental results, as shown in Fig. 12, with errors induced by obvious simplifications, such as linearizing the load-displacement curve, and neglecting the distal parts. However, as the joint force dominates the dynamic performance, the major difference across the three joint conditions has been revealed with this simple model.

REFERENCES

[1] S. A. Burden, T. Libby, K. Jayaram, S. Sponberg, and J. M. Donelan, "Why animals can outrun robots," *Sci. Robot.*, vol. 9, no. 89, 2024, Art. no. eadi9754.

[2] D. Kulić, G. Venture, K. Yamane, E. Demircan, I. Mizuuchi, and K. Mombaur, "Anthropomorphic movement analysis and synthesis: A survey of methods and applications," *IEEE Trans. Robot.*, vol. 32, no. 4, pp. 776–795, Aug. 2016.

[3] M. Santello, "Review of motor control mechanisms underlying impact absorption from falls," *Gait Posture*, vol. 21, no. 1, pp. 85–94, 2005.

[4] C. T. Moritz and C. T. Farley, "Passive dynamics change leg mechanics for an unexpected surface during human hopping," *J. Appl. Physiol.*, vol. 97, no. 4, pp. 1313–1322, 2004.

[5] T. Horita, P. Komi, C. Nicol, and H. Kyröläinen, "Interaction between pre-landing activities and stiffness regulation of the knee joint musculoskeletal system in the drop jump: Implications to performance," *Eur. J. Appl. Physiol.*, vol. 88, pp. 76–84, 2002.

[6] A. Rosendo, X. Liu, M. Shimizu, and K. Hosoda, "Stretch reflex improves rolling stability during hopping of a decerebrate biped system," *Bioinspiration Biomimetics*, vol. 10, no. 1, 2015, Art. no. 016008.

[7] R. M. Alexander, *Principles of Animal Locomotion.* Princeton, NJ, USA: Princeton Univ. Press, 2003.

[8] M. A. Daley and A. A. Biewener, "Running over rough terrain reveals limb control for intrinsic stability," *Proc. Nat. Acad. Sci.*, vol. 103, no. 42, pp. 15681–15686, 2006.

[9] M. W. Whittle, "Generation and attenuation of transient impulsive forces beneath the foot: A review," *Gait Posture*, vol. 10, no. 3, pp. 264–275, 1999.

[10] T. R. Derrick, J. Hamill, and G. E. Caldwell, "Energy absorption of impacts during running at various stride lengths.," *Med. Sci. Sports Exercise*, vol. 30, no. 1, pp. 128–135, 1998.

[11] D. E. Lieberman et al., "Foot strike patterns and collision forces in habitually barefoot versus shod runners," *Nature*, vol. 463, no. 7280, pp. 531–535, 2010.

[12] P. M. Wensing, M. Posa, Y. Hu, A. Escande, N. Mansard, and A. Del Prete, "Optimization-based control for dynamic legged robots," *IEEE Trans. Robot.*, vol. 40, pp. 43–63, 2024.

[13] D. Hoeller, N. Rudin, D. Sako, and M. Hutter, "Anymal parkour: Learning agile navigation for quadrupedal robots," *Sci. Robot.*, vol. 9, no. 88, 2024, Art. no. eadi7566.

[14] L. Han et al., "Lifelike agility and play in quadrupedal robots using reinforcement learning and generative pre-trained models," *Nat. Mach. Intell.*, vol. 6, no. 7, pp. 787–798, 2024.

[15] Y. Kim et al., "Not only rewards but also constraints: Applications on legged robot locomotion," *IEEE Trans. Robot.*, vol. 40, pp. 2984–3003, 2024.

[16] A. De Santis, B. Siciliano, A. De Luca, and A. Bicchi, "An atlas of physical human–robot interaction," *Mech. Mach. Theory*, vol. 43, no. 3, pp. 253–270, 2008.

[17] S. Haddadin and E. Croft, "Physical human–robot interaction," in *Springer Handbook of Robotics.* Cham, Switzerland: Springer, 2016, pp. 1835–1874.

[18] S. Haddadin, A. De Luca, and A. Albu-Schäffer, "Robot collisions: A survey on detection, isolation, and identification," *IEEE Trans. Robot.*, vol. 33, no. 6, pp. 1292–1312, Dec. 2017.

[19] L. Wang, A. D. Ames, and M. Egerstedt, "Safety barrier certificates for collisions-free multirobot systems," *IEEE Trans. Robot.*, vol. 33, no. 3, pp. 661–674, Jun. 2017.

[20] P. M. Wensing, A. Wang, S. Seok, D. Otten, J. Lang, and S. Kim, "Proprioceptive actuator design in the MIT cheetah: Impact mitigation and high-bandwidth physical interaction for dynamic legged robots," *IEEE Trans. Robot.*, vol. 33, no. 3, pp. 509–522, Jun. 2017.

[21] C. Della Santina, M. G. Catalano, A. Bicchi, M. Ang, O. Khatib, and B. Siciliano, "Soft robots," *Encyclopedia Robot.*, vol. 489, pp. 1–15, 2020.

[22] M. Calisti, G. Picardi, and C. Laschi, "Fundamentals of soft robot locomotion," *J. R. Soc. Interface*, vol. 14, no. 130, 2017, Art. no. 20170101.

[23] J. Winters, L. Stark, and A.-H. Seif-Naraghi, "An analysis of the sources of musculoskeletal system impedance," *J. Biomech.*, vol. 21, no. 12, pp. 1011–1025, 1988.

[24] Y. Fukuda et al., "Impact load transmission of the knee joint-influence of leg alignment and the role of meniscus and articular cartilage," *Clin. Biomech.*, vol. 15, no. 7, pp. 516–521, 2000.

[25] T. J. Roberts and E. Azizi, "Flexible mechanisms: The diverse roles of biological springs in vertebrate movement," *J. Exp. Biol.*, vol. 214, no. 3, pp. 353–361, 2011.

[26] M. Nordin, *Basic Biomechanics of the Musculoskeletal System*, vol. 2. Philadelphia, PA, USA: Lippincott Williams & Wilkins, 2001, pp. 267–275.

[27] R. F. LaPrade, E. A. Arendt, A. Getgood, and S. C. Faucett, *The Menisci: A Comprehensive Review of Their Anatomy, Biomechanical Function and Surgical Treatment.* Berlin, Germany: Springer, 2017.

[28] I. D. McDermott, S. D. Masouros, and A. A. Amis, "Biomechanics of the menisci of the knee," *Curr. Orthopaedics*, vol. 22, no. 3, pp. 193–201, 2008.

[29] R. F. LaPrade and J. Chahla, *Evidence-Based Management of Complex Knee Injuries E-Book: Restoring the Anatomy to Achieve Best Outcomes.* Amsterdam, Netherlands: Elsevier Health Sciences, 2020.

[30] A. Hoshino and W. Wallace, "Impact-absorbing properties of the human knee," *J. Bone Joint Surg. Brit. Vol.*, vol. 69, no. 5, pp. 807–811, 1987.

[31] J. Zhang et al., "Robotic artificial muscles: Current progress and future perspectives," *IEEE Trans. Robot.*, vol. 35, no. 3, pp. 761–781, Jun. 2019.

[32] M. Duduta, E. Hajiesmaili, H. Zhao, R. J. Wood, and D. R. Clarke, "Realizing the potential of dielectric elastomer artificial muscles," in *Proc. Nat. Acad. Sci.*, vol. 116, no. 7, pp. 2476–2481, 2019.

[33] M. Kanik et al., "Strain-programmable fiber-based artificial muscle," *Science*, vol. 365, no. 6449, pp. 145–150, 2019.

[34] S. M. Mirvakili, D. Sim, I. W. Hunter, and R. Langer, "Actuation of untethered pneumatic artificial muscles and soft robots using magnetically induced liquid-to-gas phase transitions," *Sci. Robot.*, vol. 5, no. 41, 2020, Art. no. eaaz4239.

[35] H. Zhao, A. M. Hussain, M. Duduta, D. M. Vogt, R. J. Wood, and D. R. Clarke, "Compact dielectric elastomer linear actuators," *Adv. Funct. Mater.*, vol. 28, no. 42, 2018, Art. no. 1804328.

[36] L. Liow et al., "A compliant robotic leg based on fibre jamming," *IEEE Trans. Robot.*, vol. 40, pp. 4578–4597, 2024.

[37] Z. Lin, Q. Shao, X.-J. Liu, and H. Zhao, "An anthropomorphic musculoskeletal system with soft joint and multifilament pneumatic artificial muscles," *Adv. Intell. Syst.*, vol. 4, no. 10, 2022, Art. no. 2200126.

[38] H. Yang, G. Wei, and L. Ren, "Enhancing the performance of a biomimetic robotic elbow-and-forearm system through bionics-inspired optimization," *IEEE Trans. Robot.*, vol. 40, pp. 2692–2711, 2024.

[39] L. Yang and Z. Zhao, "A meniscus-like structure in anthropomorphic joints to attenuate impacts," *IEEE Trans. Robot.*, vol. 40, pp. 3109–3126, 2024.

[40] Z.-Z. Zhang et al., "Orchestrated biomechanical, structural, and biochemical stimuli for engineering anisotropic meniscus," *Sci. Transl. Med.*, vol. 11, no. 487, 2019, Art. no. eaao0750.

[41] E. Krimsky and S. H. Collins, "Elastic energy-recycling actuators for efficient robots," *Sci. Robot.*, vol. 9, no. 88, 2024, Art. no. eadj7246.

[42] J. Choi, S. Hong, W. Lee, S. Kang, and M. Kim, "A robot joint with variable stiffness using leaf springs," *IEEE Trans. Robot.*, vol. 27, no. 2, pp. 229–238, Apr. 2011.

[43] C. W. Mathews and D. J. Braun, "Design of parallel variable stiffness actuators," *IEEE Trans. Robot.*, vol. 39, no. 1, pp. 768–782, Feb. 2023.

[44] E. J. Rouse, L. M. Mooney, and H. M. Herr, "Clutchable series-elastic actuator: Implications for prosthetic knee design," *Int. J. Robot. Res.*, vol. 33, no. 13, pp. 1611–1625, 2014.

[45] D. W. Haldane, M. M. Plecnik, J. K. Yim, and R. S. Fearing, "Robotic vertical jumping agility via series-elastic power modulation," *Sci. Robot.*, vol. 1, no. 1, 2016, Art. no. eaag2048.

[46] J. Bian and X. Jing, "Analysis and design of a novel and compact X-structured vibration isolation mount (X-mount) with wider quasi-zero-stiffness range," *Nonlinear Dyn.*, vol. 101, no. 4, pp. 2195–2222, 2020.

[47] G. Yan, H.-X. Zou, S. Wang, L.-C. Zhao, Z.-Y. Wu, and W.-M. Zhang, "Bio-inspired vibration isolation: Methodology and design," *Appl. Mech. Rev.*, vol. 73, no. 2, 2021, Art. no. 020801.

[48] Z. Wu, X. Jing, J. Bian, F. Li, and R. Allen, "Vibration isolation by exploring bio-inspired structural nonlinearity," *Bioinspiration Biomimetics*, vol. 10, no. 5, 2015, Art. no. 056015.

[49] A. C. Etoundi, S. C. Burgess, and R. Vaidyanathan, "A bio-inspired condylar hinge for robotic limbs," *J. Mech. Robot.*, vol. 5, no. 3, 2013, Art. no. 031011.

[50] W. Liang et al., "A bioinspired robotic knee with controlled joint surfaces and adjustable ligaments," *Bioinspiration Biomimetics*, vol. 17, no. 6, 2022, Art. no. 066006.

[51] P. Flores and J. Ambrósio, "Revolute joints with clearance in multibody systems," *Comput. Struct.*, vol. 82, no. 17—19, pp. 1359–1369, 2004.

[52] L. C. Rome, L. Flynn, and T. D. Yoo, "Rubber bands reduce the cost of carrying loads," *Nature*, vol. 444, no. 7122, pp. 1023–1024, 2006.

[53] R. Chaichaowarat, D. F. P. Granados, J. Kinugawa, and K. Kosuge, "Passive knee exoskeleton using torsion spring for cycling assistance," in *Proc. IEEE Int. Conf. Intell. Robots Syst.*, 2017, pp. 3069–3074.

[54] M. Tran, L. Gabert, S. Hood, and T. Lenzi, "A lightweight robotic leg prosthesis replicating the biomechanics of the knee, ankle, and toe joint," *Sci. Robot.*, vol. 7, no. 72, 2022, Art. no. eabo3996.

[55] S. Burgess, "A review of linkage mechanisms in animal joints and related bioinspired designs," *Bioinspiration Biomimetics*, vol. 16, no. 4, 2021, Art. no. 041001.

[56] B. Celebi, M. Yalcin, and V. Patoglu, "AssistOn-knee: A self-aligning knee exoskeleton," in *Proc. IEEE Int. Conf. Intell. Robots Syst.*, 2013, pp. 996–1002.

[57] D. A. Winter, *Biomechanics and Motor Control of Human Movement.* Hoboken, NJ, USA: Wiley, 2009.

Lianxin Yang (Member, IEEE) received the B.S. degree in engineering mechanics and the Ph.D. degree in mechanical engineering from Tsinghua University, Beijing, China, in 2016 and 2021, respectively.

She is currently an Associate Professor with the School of Automation Science and Electrical Engineering, Beihang University, Beijing, China. From 2021 to 2025, she was a Postdoc with the School of Aerospace Engineering, Tsinghua University. Her research interests include bionic robotics, locomotion, and biomechanics.

Xinyan Li received the B.E. degree in guidance, navigation, and control technology from the University of Electronic Science and Technology of China, Chengdu, China, in 2023. She is currently working toward the Ph.D. degree in dynamics and control with the School of Aerospace Engineering, Tsinghua University, Beijing, China.

Her research interests include computational multibody dynamics and bionic robotics.

Tianyu Zhao received the B.E. degree in aeronautics and astronautics engineering in 2023 from Tsinghua University, Beijing, China, where he is currently working toward the Ph.D. degree in dynamics and control with the School of Aerospace Engineering.

His research interests include mechanisms and autopilots in flapping aerial drones.

Zhihua Zhao received the B.S. and M.S. degrees in solid mechanics and the Ph.D. degree in dynamics and control from Tsinghua University, Beijing, China, in 2003, 2006, and 2011, respectively.

He is currently an Associate Professor with the School of Aerospace Engineering at Tsinghua University. His research interests include bionic air vehicles, multibody dynamics, and deployment mechanisms.